Graphene billiards with fourfold symmetry

Weihua Zhang [1,2,*] and Barbara Dietz [2,3,1,†]

[1] *Lanzhou Center for Theoretical Physics, and the Gansu Provincial Key Laboratories of Theoretical Physics and of Quantum Theory and Applications of MoE, Lanzhou University, Lanzhou, Gansu 730000, China*

[2] *Center for Theoretical Physics of Complex Systems, Institute for Basic Science (IBS), Daejeon 34126, Republic of Korea*

[3] *Basic Science Program, Korea University of Science and Technology (UST), Daejeon 34113, Republic of Korea*

(Received 14 August 2023; accepted 27 September 2023; published 10 October 2023)

We report on the realization of a graphene billiard with a fourfold rotational symmetry, which has the shape of a billiard with chaotic classical dynamics. The eigenstates are separated according to their transformation properties under rotation by $\frac{\pi}{2}$ into four symmetry classes. These subspectra can be divided into regions around the band edges, where they are governed by the nonrelativistic Schrödinger equation, and a region of low energy-excitations around zero energy, that exhibit a linear dispersion relation and are described by the relativistic Dirac equation for a spin-1/2 quasiparticle. We analyze the spectral properties in these parts and compare them with those for nonrelativistic quantum billiards and relativistic neutrino billiards. In both regions the spectral properties conform with those of nonrelativistic quantum billiards of corresponding shape. Furthermore, we compute wave functions in configurational space and momentum distributions in quasimomentum space and find that the first Brillouin zone is formed by two hexagonal ones that are rotated by 30° with respect to each other. Namely, in the relativistic region the momentum distributions are localized at or near the 12 Dirac points at the corners of these hexagons. At the Van Hove singularities, which separate the nonrelativistic and relativistic regions, they are localized along the isofrequency lines that connect the six saddle points at the centers between two corners for each hexagon. We propose a design of a microwave photonic crystal for the experimental modeling of graphene billiards with fourfold symmetry and present numerical results for its properties.

DOI: 10.1103/PhysRevResearch.5.043028

I. INTRODUCTION

Billiards are a paradigm model for the study of aspects of quantum chaos. A classical billiard (CB) consists of a point particle which moves freely inside a bounded two-dimensional domain and is reflected specularly at the boundary. Its dynamics is determined by the shape of the domain [1–3]. The eigenstates of the corresponding nonrelativistic quantum billiard (QB) are the solutions of the Schrödinger equation for a free particle with Dirichlet boundary conditions (BCs). In 1987, Berry and Mondragon proposed relativistic neutrino billiards [4] (NBs) that are governed by the Dirac equation for a massless spin-1/2 particle, which is confined to the billiard domain by imposing the BC that there is no outgoing flow. Another type of billiards, which may exhibit nonrelativistic or relativistic features depending on energy, are graphene billiards (GBs) [5–15]. They are constructed by cutting their shape out of an extended honeycomb lattice and are used to emulate properties of artificial graphene flakes based on a tight-binding model (TBM) [16,17]. Around the corners of the hexagonal Brillouin zone, where the conduction band and valence band touch each other conically, the energy excitations of graphene are well described by the Dirac equation for massless spin-1/2 particles [6,7,11,13,18]. The associated BCs on the spinor components in a GB were formulated in Refs. [19–21]. The touch points are referred to as "Dirac points." The conical shape originates from the honeycomb-lattice structure [22], which is formed by two interpenetrating triangular sublattices. This led to the realization of numerous experimental "artificial-graphene" realizations [23–40]. We modeled rectangular, Africa-shaped, and threefold-symmetric GBs experimentally with flat superconducting microwave photonic crystals [41–45], named Dirac billiards (DBs) because their energy spectra exhibit Dirac points around which they exhibit relativistic phenomena.

Key aspects of quantum chaos are the properties of the wave functions and the fluctuation properties in the eigenvalue spectra of a quantum system, as well as their connection to the properties of the dynamics of the corresponding classical system. Berry and Tabor showed in Ref. [46] that the spectral properties of typical integrable systems [47] agree well with those of Poissonian random numbers. According to a conjecture by Bohigas, Giannoni, and Schmit [48] (BGS) the spectral properties of quantum systems with a chaotic classical dynamics coincide with those of random matrices from the Gaussian ensembles (GEs) of the corresponding universality

*zhangwh2018@gmail.com
†bdietzp@gmail.com

class [49–52]; see also Refs. [53,54]. The appropriate GEs for quantum systems with preserved and violated time-reversal invariance are the Gaussian orthogonal ensemble (GOE) and the Gaussian unitary ensemble (GUE), respectively. Since the Dirac Hamiltonian associated with NBs is not invariant under time reversal, the spectral properties of typical NBs with the shapes of chaotic CBs and no geometric symmetry coincide with those of random matrices from the GUE. The spectral properties of GBs with such shapes were expected to be similar to those of NBs in the valley regions around the Dirac points, because there they are governed by the same wave equations. This was confirmed in experiments with graphene quantum dots [55,56] with the shape of a chaotic billiard [10]. However, numerical [57–60] and experimental investigations [41,42,44,45] with GBs yielded the finding that they conform with GOE statistics. The discrepancies were attributed to the BCs [57,59,60] and to backscattering at the boundary, which leads to a mixing of valley states corresponding to the two independent Dirac points associated with the two triangular sublattices. In Refs. [61,62], GBs and NBs with shapes of CBs with an integrable dynamics are presented whose spectral properties do not agree with Poissonian statistics but with GOE or intermediate statistics.

There also exist nonrelativistic QBs with certain symmetry properties, which do not comply with the BGS conjecture. Examples are billiards with a threefold rotational symmetry [63–65] or, generally, an M-fold rotational symmetry, a unidirectional classical dynamics [66–69], or nanoelectromechanical systems consisting of a circular quantum dot on a suspended nanoscopic dielectric plate [70,71]. These are time-reversal invariant systems; however, part of their subspectra exhibit GUE statistics. In Ref. [72] we considered a GB with threefold (C_3) rotational symmetry, which was investigated experimentally in Ref. [45], and determined that properties of their eigenvalues and eigenfunctions agree with those of the QB of corresponding shape; that is, we found GUE statistics for two of the three subspectra. Such GBs can be constructed by cutting a graphene sheet to their shape because the symmetry properties comply with those of the hexagonal lattice. It is not possible to realize in this way GBs with a fourfold rotational symmetry. The objective of this paper is to demonstrate that GBs with that symmetry property can still be constructed and to investigate and compare properties of their eigenvalues and eigenfunctions with those of the nonrelativistic QB and relativistic NB of corresponding shape. We obtain the GBs by cutting four identical sheets with the shape of a fundamental domain out of a graphene sheet and gluing them together and demonstrate that the GBs exhibit the features of a quantum system with fourfold rotational symmetry. In Sec. II we review the properties of relativistic and nonrelativistic QBs with fourfold symmetry. In Sec. III we present the results for the corresponding GB, and in Sec. IV we propose an experimental realization based on a microwave photonic crystal, i.e., a DB of corresponding shape. Finally, we discuss our findings in Sec. V.

II. BILLIARDS WITH FOURFOLD SYMMETRY

A classical billiard (CB) refers to a pointlike particle confined in a bounded two-dimensional domain, where it moves freely and is reflected specularly at the boundary. We define the domain Ω of the billiard in a Cartesian coordinate system in polar coordinates, $\boldsymbol{r} = [x(r,\varphi), y(r,\varphi)]$, or in the complex plane, $w(r,\varphi) = x(r,\varphi) + iy(r,\varphi)$, with $\varphi \in [0, 2\pi)$, $r \in [0, r_0]$ with the boundary $\partial\Omega$ at $r = r_0$.

The eigenfunctions $\psi(r,\varphi)$ of nonrelativistic QBs and the electric-field strength of microwave billiards (MBs) [73–75] are governed by the Schrödinger equation and the Helmholtz equation, respectively, with Dirichlet BCs along $\partial\Omega$,

$$\begin{aligned} \hat{H}\psi_m(r,\varphi) &= -\Delta_{(r,\varphi)}\psi_m(r,\varphi) = k_m^2\psi_m(r,\varphi), \\ \psi_m(r,\varphi)|_{r=r_0} &= 0. \end{aligned} \tag{1}$$

The eigenenergies $E_m = k_m^2$ of the Hamiltonian $\hat{H}$ are given in terms of the wave numbers k_m. These are related to the eigenfrequencies f_m of the corresponding MB through the relation $k_m = 2\pi f_m/c$, where c denotes the velocity of light in a vacuum.

Neutrino billiards were introduced in Ref. [4]. They are governed by the Weyl equation [76] for a noninteracting spin-1/2 particle of mass zero, referred to as the Dirac equation in Ref. [4],

$$\hat{\boldsymbol{H}}_D\boldsymbol{\psi} = c\hat{\boldsymbol{\sigma}}\cdot\hat{\boldsymbol{p}}\boldsymbol{\psi} = E\boldsymbol{\psi}, \quad \boldsymbol{\psi} = \begin{pmatrix}\psi_1\\ \psi_2\end{pmatrix}, \tag{2}$$

with $\hat{\boldsymbol{p}} = -i\hbar\nabla$ being the momentum of the particle, $\hat{\boldsymbol{H}}_D$ denoting the Dirac Hamiltonian, and $\hat{\boldsymbol{\sigma}} = (\hat{\sigma}_x, \hat{\sigma}_y)$, where $\hat{\sigma}_{x,y,z}$ are the Pauli matrices. Furthermore, $E = \hbar ck$ is the energy of the particle, where k is the free-space wave vector. In Ref. [4] only this ultrarelativistic case was considered, which was extended to massive NBs in Refs. [45,72,77]. The particle is confined to the billiard domain by requiring that the normal component of the local current, that is, of the expectation value of the current operator $\hat{\boldsymbol{u}} = \nabla_{\boldsymbol{p}}\hat{\boldsymbol{H}}_D = c\hat{\boldsymbol{\sigma}}$, $\boldsymbol{n}\cdot\boldsymbol{u}(\boldsymbol{r}) = c\boldsymbol{n}\cdot[\boldsymbol{\psi}^\dagger\hat{\boldsymbol{\sigma}}\boldsymbol{\psi}]$ is zero along the boundary, leading to the BC [4]

$$\psi_2(\varphi) = i\mu e^{i\alpha(\varphi)}\psi_1(\varphi). \tag{3}$$

Here, $\alpha(\varphi)$ is the angle of the outward-pointing normal vector $\boldsymbol{n} = [\cos\alpha(\varphi), \sin\alpha(\varphi)]$ at $w(r_0,\varphi)$ with respect to the x axis, and $\mu = \pm 1$ determines the rotational direction of the current at the boundary. We use $\mu = 1$ in the following.

In this paper we investigate the spectral properties and properties of the wave functions and momentum distributions of the symmetry-projected eigenstates of a GB with fourfold symmetry, implying that it is invariant under $\varphi \to \varphi + \frac{\pi}{2}$, and also analyze those of the corresponding QB and NB. A further requirement on the billiard shape is that the dynamics of the CB is fully chaotic. Thus, in order to avoid the occurrence of families of bouncing-ball-like orbits, i.e., continuous sets of neutral orbits, which yield nongeneric contributions to the spectral properties [3,78,79], the boundary should not comprise straight-line parts. Furthermore, bulges should be designed such that orbits cannot be trapped in them. The shape shown in Fig. 1 complies with these requirements. The domain Ω of the billiard is defined by the parametrization

$$w(r,\varphi) = r[1 + 0.1\cos(4\varphi) - 0.1\sin(8\varphi)]e^{i\varphi}, \quad r \leqslant r_0, \tag{4}$$

where in the numerical simulations $r_0 = 3$.

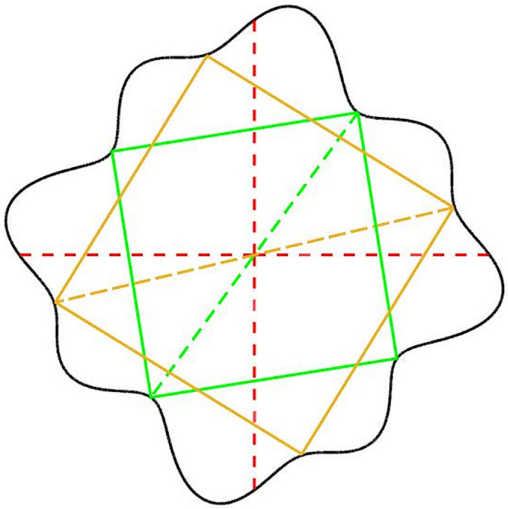

FIG. 1. Shape of the fourfold-symmetric billiard. The domain can be divided into four fundamental domains that are mapped onto each other under rotation by $\frac{\pi}{2}$. We use the subdivision indicated by the red dashed lines for the construction of the GB. The shortest connected periodic orbit is a square orbit of length $\tilde{l}_s \simeq 1.165 \times 4r_0$ (green solid lines). A second square orbit of length $\tilde{l} \simeq 1.355 \times 4r_0$ is exhibited (orange solid lines). Furthermore, the diameters of the two orbits with lengths $1.646 \times 2r_0$ (green dashed line) and $1.916 \times 2r_0$ (orange dashed line) are shown.

Generally, M-fold symmetry of the boundary of a billiard implies that $w(\varphi) \equiv w(r_0, \varphi)$ has the periodicity properties

$$w\left(\varphi + \lambda\frac{2\pi}{M}\right) = e^{i\lambda\frac{2\pi}{M}} w(\varphi), \tag{5}$$

$$e^{i\alpha\left(\varphi+\lambda\frac{2\pi}{M}\right)} = e^{i\lambda\frac{2\pi}{M}} e^{i\alpha(\varphi)}, \tag{6}$$

with $\lambda = 0, 1, 2, \ldots, M-1$.

The eigenstates of the corresponding nonrelativistic QB can be classified into M subspaces labeled by $l = 0, \ldots, M-1$ according to their transformation properties with respect to rotation by $\frac{2\pi}{M}$ under application of the rotation operator

$$\hat{R} = e^{i\frac{2\pi}{M}\hat{L}} \tag{7}$$

with $\hat{L}$ denoting the angular momentum operator. The symmetry-projected eigenfunctions of the QB are characterized by the property

$$\hat{R}^\lambda \psi_m^{(l)}(r, \varphi) = \psi_m^{(l)}\left(r, \varphi - \frac{2\pi}{M}\lambda\right) = e^{il\frac{2\pi}{M}\lambda} \psi_m^{(l)}(r, \varphi). \tag{8}$$

Furthermore, they are real for $l = 0$ and also for $l = M/2$ for even M, that is, invariant under the time-reversal operator $\hat{T} = \hat{\mathcal{C}}$ with $\hat{\mathcal{C}}$ denoting the complex conjugation operator [52], whereas for $l \neq 0, M/2$ they are complex and

$$\hat{T}\psi_m^{(l)}(r, \varphi) = \psi_m^{(M-l)}(r, \varphi). \tag{9}$$

Thus, because the billiard system is invariant under $\mathcal{T}$ violation, $\psi_m^{(l)}(r, \varphi)$ and $\psi_m^{(M-l)}(r, \varphi)$ are eigenfunctions with the same eigenvalue k_m^2. Here, we used the fact that

$$\hat{\mathcal{C}}\psi_m^{(l)}\left(r, \varphi - \frac{2\pi}{M}\lambda\right) = e^{-il\frac{2\pi}{M}\lambda}\left[\psi_m^{(l)}(r, \varphi)\right]^* = e^{i(M-l)\frac{2\pi}{M}\lambda}\left[\psi_m^{(l)}(r, \varphi)\right]^* \tag{10}$$

implying that $[\psi_m^{(l)}(r, \varphi)]^* = \psi_m^{(M-l)}(r, \varphi)$. Accordingly, the eigenvalue spectrum can be separated into nondegenerate eigenvalues (singlets) with $l = 0, \frac{M}{2}$ and pairwise degenerate ones (doublets) with labels $l, M-l$. If the corresponding classical dynamics is chaotic and if the billiard boundary has no additional geometric symmetries, the spectral properties of the singlets show GOE behavior, while those of the doublet partners exhibit GUE statistics [63].

The eigenstates of the corresponding NB can also be grouped according to their transformation properties under a rotation by $\frac{2\pi}{M}$ into $M-1$ subspaces [63,80–82],

$$\hat{\boldsymbol{R}}^\lambda \psi_{1,2}^{(l)}(\boldsymbol{r}) = e^{il\frac{2\pi}{M}\lambda} \psi_{1,2}^{(l)}(\boldsymbol{r}), \quad \lambda = 0, 1, \ldots, M-1. \tag{11}$$

However, the components of the spinor eigenfunctions belong to different subspaces [72,83]. Namely, if the first component of the mth spinor eigenfunction belongs to the subspace l,

$$\hat{R}\psi_{1,m}(\boldsymbol{r}) = e^{il\frac{2\pi}{M}} \psi_{1,m}(\boldsymbol{r}), \tag{12}$$

the second one belongs to the subspace $\tilde{l} = (l-1)$,

$$\hat{R}\psi_{2,m}(\boldsymbol{r}) = e^{i(l-1)\frac{2\pi}{M}} \psi_{2,m}(\boldsymbol{r}), \tag{13}$$

where $\tilde{l} = -1$ corresponds to $l = M-1$. This intermingling of symmetry properties originates from the additional spin degree of freedom [72,83]. We denote in the following the symmetry-reduced eigenstates by the label l corresponding to the subspace of the first spinor component. The spectral properties of the NB are well described by the GUE for all subspaces, if it has the shape of a billiard with chaotic dynamics and no mirror symmetries. Furthermore, since $\mathcal{T}$ invariance is violated, the eigenvalues belonging to subspaces l and $M-l$ are not degenerate.

For the analysis of spectral properties the ordered eigenvalues k_m with $k_1 \leqslant k_2 \leqslant \cdots$ were unfolded to mean spacing unity by replacing them by the smooth part of the integrated spectral density, $\epsilon_m = N^{\text{smooth}}(k_m)$. For QBs it is given by Weyl's formula [84], $N^{\text{Weyl}}(k_m) = \frac{\mathcal{A}}{4\pi}k_m^2 - \frac{\mathcal{L}}{4\pi}k_m + C_0$, with $\mathcal{A}$ and $\mathcal{L}$ denoting the area and perimeter of the billiard, respectively. For massless NBs the Weyl formula is the same, except that the perimeter term is absent [4]. We computed the nearest-neighbor spacing distribution $P(s)$, the integrated nearest-neighbor spacing distribution $I(s)$, the number variance $\Sigma^2(L)$, and the rigidity $\Delta_3(L)$ of the spectrum [49]. Furthermore, we analyzed distributions of the ratios [85,86] of consecutive spacings between nearest neighbors, $r_j = \frac{\epsilon_{j+1}-\epsilon_j}{\epsilon_j-\epsilon_{j-1}}$, which are dimensionless so that no unfolding is needed [85–87].

We computed, for each symmetry class of the QB and NB, 5000 eigenvalues using the corresponding boundary-integral method [4,77,88,89]; see Appendix A. Examples of wave functions are shown in Fig. 2 for $l = 0, 1, 2$. For $l = 3$ they are indistinguishable from those for $l = 1$. Generally, the wave functions are spread over the whole billiard area; however, some exhibit a cross- or square-shaped pattern of increased intensity, as illustrated in these examples. However, this scarring is not as pronounced as, e.g., in the threefold-symmetric billiards considered in Ref. [72]. This explains why deviations of the spectral properties from random-matrix theory (RMT) are small in the present case compared with those observed

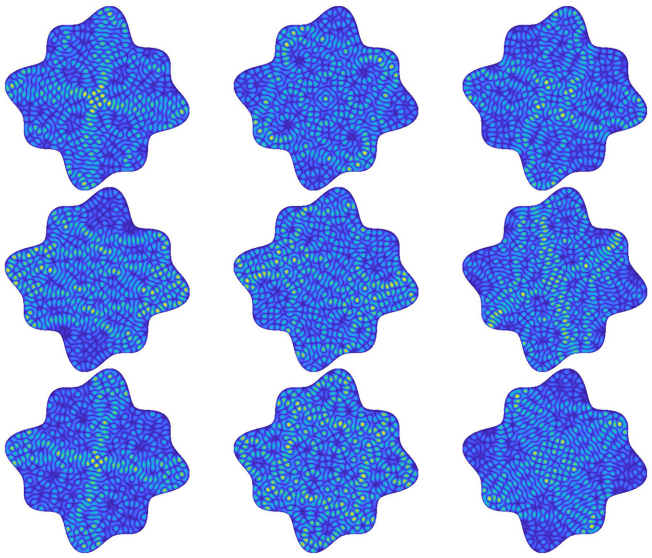

FIG. 2. Intensity distributions of the wave functions of the QB for the symmetry-reduced eigenstates with $l = 0$ and $n = 207, 209, 211$ (first row), $l = 1$ and $n = 211, 216, 217$ (second row), and $l = 2$ and $n = 205, 207, 215$ (third row).

in that paper. These are shown in Fig. 3 for the QB and its symmetry-projected eigenstates labeled by $l = 0, 1, 2, 3$. The eigenvalues corresponding to $l = 1$ and $l = 3$ are degenerate. Therefore we only show spectral properties for the case $l = 1$. They agree well with the GOE for $l = 0, 2$ and with the GUE for $l = 1$. For $l = 0$, slight deviations are observed for $L \gtrsim 3$ for $\Sigma^2(L)$ and $L \gtrsim 12$ for $\Delta_3(L)$, whereas no deviations from the predicted RMT curves are observed for $l = 1$. This indicates that especially for $l = 0$ there are nonuniversal contributions from states that are scarred along, e.g., the shortest connected periodic orbit, shown in Fig. 1, or a cross orbit, that are absent for $l = 3$. For the threefold QB and NB studied in Ref. [45,72], such contributions led to clear deviations from RMT predictions. These, however, could be extracted from the fluctuating part of the integrated spectral density, where they are visible as slow oscillations that can be determined by employing length spectra [79,90]. We also include the results for the complete level sequence comprising the eigenvalues corresponding to eigenstates with $l = 0, 1, 2$. These are compared with an RMT model consisting of block-diagonal matrices of the same dimensions, where two blocks are drawn from the GOE and one from the GUE. Agreement is very good for the short-range correlations, and only small deviations are observed for the long-range correlations.

Figure 4 shows the spectral properties for the NB and its symmetry-projected states. Shown are the results for $l = 0, 1, 2, 3$. The curves lie on top of each other and agree well with the GUE curves. Furthermore, curves obtained from the complete spectrum agree well with the RMT model of block-diagonal matrices of the same dimensions comprising four blocks of matrices drawn from the GUE. In Fig. 5 are plotted intensity distributions of the local current exhibiting similar patterns to the wave-function intensities of the QB in Fig. 2. Like in the nonrelativistic QB, it is generally spread over the whole billiard area. Shown are examples where the local

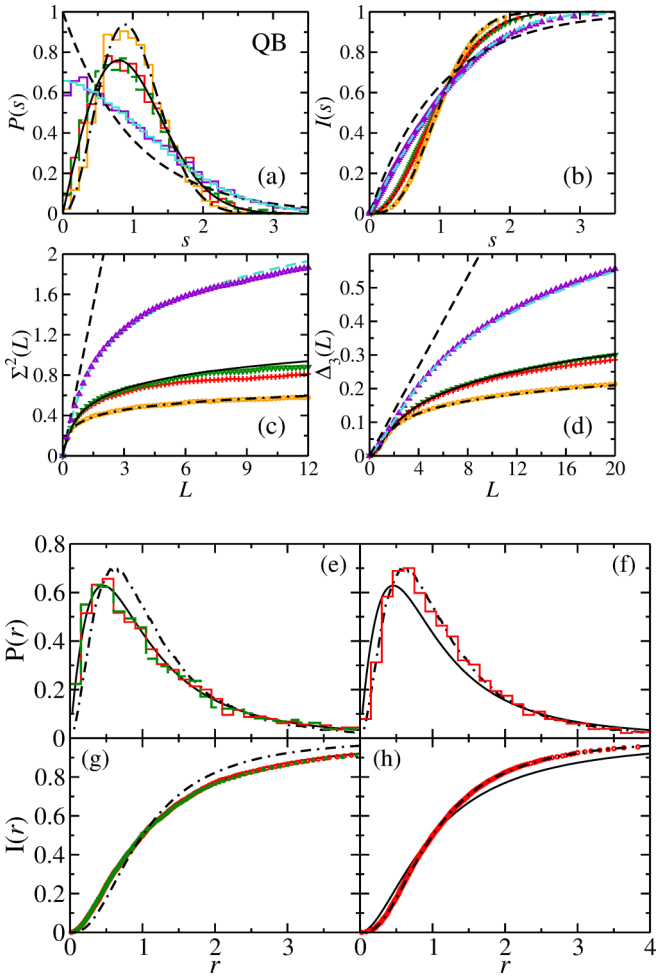

FIG. 3. (a)–(d) Spectral properties of the QB (violet histogram and upward pointing triangles) and its symmetry-projected eigenstates (red histogram and pluses, $l = 0$; orange histogram and circles, $l = 1$; green histogram and inverted triangles, $l = 2$). They are compared with the results for GOE (black solid curves), Poisson (black dashed curves), and GUE (black dash-dotted curves) statistics and a superposition of one GUE and two GOEs (turquoise histogram and dashed curves). (e)–(h) Ratio distributions $P(r)$ and cumulative ratio distributions $I(r)$ for the symmetry-projected eigenstates of the QB with $l = 0$ (red histogram and circles) and $l = 2$ (green histogram and squares) [(e) and (g)] and $l = 1$ (red histogram and circles) [(f) and (h)]. They are compared with the results for GOE (black solid curves) and GUE (black dash-dotted curves) statistics.

current pattern exhibits increased intensity around a cross or square similar to those shown in Fig. 2. However, the effect of such states on the spectral properties is much smaller than for the QB.

In Fig. 6 we compare length spectra, that is, the modulus of the Fourier transform of the fluctuating part of the spectral density from wave number k to length l in units of r_0 for the complete eigenvalue sequences. That of the QB is obtained by summing over all four complex-valued symmetry-projected Fourier transforms. The length spectra exhibit peaks at the lengths of the periodic orbits of the CB of corresponding shape. Generally, in the length spectra of NBs, peaks at lengths that correspond to orbits with an odd

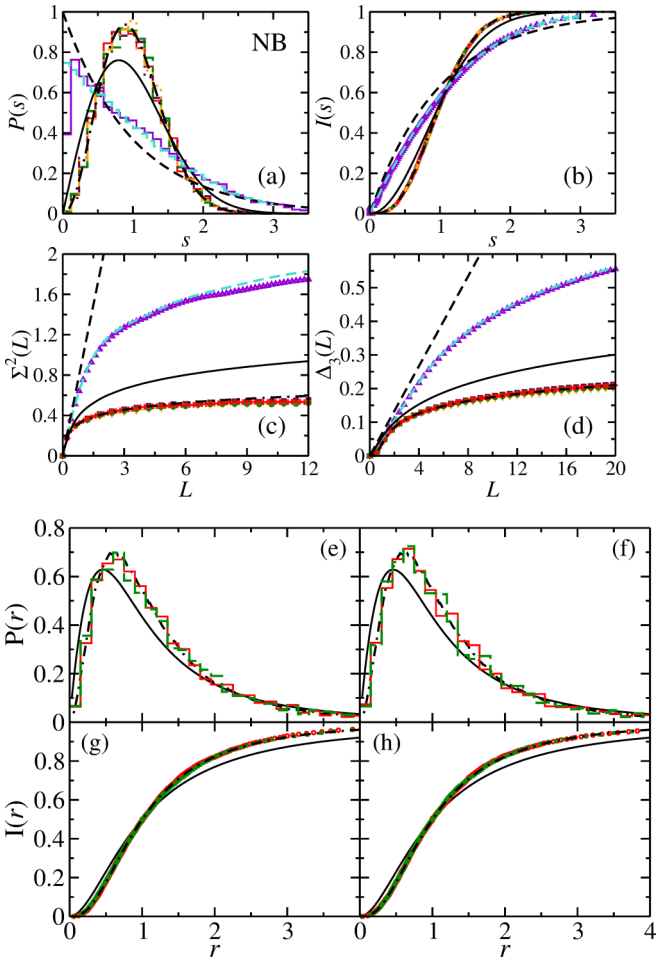

FIG. 4. (a)–(d) Spectral properties of the NB (violet histogram and upward pointing triangles) and its symmetry-projected eigenstates (red histogram and pluses, $l = 0$; green histogram and circles, $l = 1$; maroon histogram and squares, $l = 2$; orange histogram and inverted triangles, $l = 3$). They are compared with the results for GOE (black solid curves), Poisson (black dashed curves), and GUE (black dash-dotted curves) statistics and a superposition of four GUE (turquoise histogram and dashed curves). (e)–(h) Ratio distributions $P(r)$ and cumulative ratio distributions $I(r)$ for the symmetry-projected eigenstates of the NB with $l = 0$ (red histogram and circles) and $l = 2$ (green histogram and squares) [(e) and (g)] and $l = 1$ (red histogram and circles) and $l = 3$ (green histogram and squares) [(f) and (h)]. They are compared with the results for GOE (black solid curves) and GUE (black dash-dotted curves) statistics.

number of reflections at the boundary are missing [77]. For both billiards the first high peak is observed at $l/r_0 \simeq 3.49$. To understand this, we also plot in Fig. 7 the length spectra obtained from the fluctuating part of the spectral density of the symmetry-projected eigenstates. They show additional peaks at lengths which correspond to pseudo-orbits, that is, orbits that are periodic in the fundamental domains but not in the full system [81,82]. In the subspectra of the QB with $l = 0, 2$ and in all of them for the NB, the first and second peaks appear at one-quarter of the lengths of the square orbits shown as green and orange lines in Fig. 1, respectively.

Length spectra of QBs, whose classical counterpart exhibits a chaotic dynamics, have been shown to be well

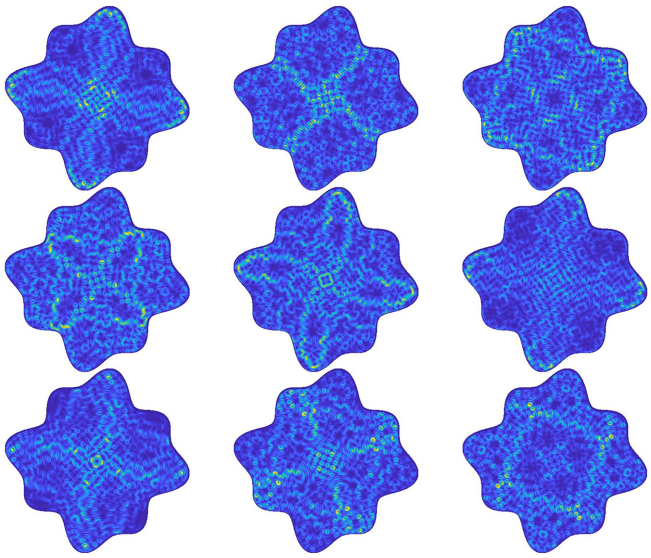

FIG. 5. Intensity distribution of the local current of the NB for the symmetry-reduced eigenstates with $l = 0$ and $n = 212, 214, 239$ (first row), $l = 1$ and $n = 206, 234, 240$ (second row), and $l = 2$ and $n = 203, 213, 230$ (third row).

reproduced by Gutzwiller's trace formula [91,92], i.e., a semiclassical approximation for the fluctuating of the spectral density in terms of a sum over periodic orbits of the CB of corresponding shape. In Ref. [81], trace formulas were derived for the symmetry-projected eigenstates of a quantum system with a discrete M-fold rotational symmetry. We extended them to NBs in Ref. [72] and provide the results for the fourfold case in Appendix B. The different contributions to the trace formulas of the QB and NB, given in Eqs. (B11) and (B12), respectively, contain phase factors of $e^{il\frac{\pi}{2}\lambda}$, $\lambda = 0, 1, 2, 3$. These lead for both billiards to the cancellation of contributions from different pseudo-orbits below $l/r_0 \simeq 3$. There the amplitudes in the trace formula, that is, the peak heights in the length spectra, corresponding to $l = 0, 2$ and $l = 1, 3$, respectively, are the same whereas the relative phases are π. To corroborate this statement, we computed the length spectrum of the full QB by using the eigenvalues for $l = 0, 1, 2$, taking into account the degeneracy of those

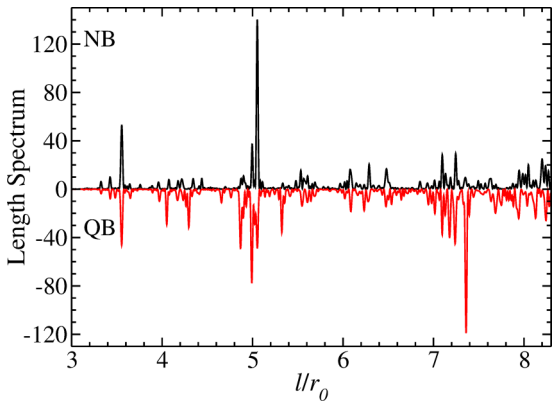

FIG. 6. Comparison of the length spectra of the NB (black) and the QB (red) obtained from the complete eigenvalue sequences.

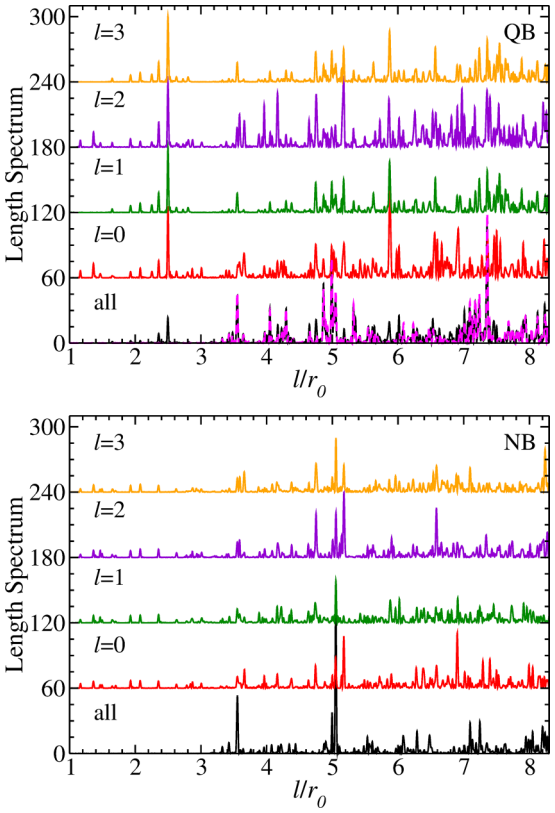

FIG. 7. Top: Comparison of the length spectra of, from bottom to top, the QB [black curve, obtained from the eigenvalues; magenta curve, obtained by summing over the Fourier transforms of $\rho^{(l)\mathrm{fluc}}(k)$] for $l = 0$ (red), $l = 1$ (green), $l = 2$ (violet), and $l = 3$ (orange). Bottom: Same as the top panel, but for the NB.

for $l = 1$ and $l = 3$, shown as the black curve in the top panel of Fig. 7, and by summing over all four complex-valued symmetry-projected Fourier transforms, shown as the magenta dashed curve in the same panel. In the latter curve, peaks below $l/r_0 \simeq 3$ disappear. Furthermore, the terms in the symmetry-projected trace formulas for the NB, given in Eq. (B12), contain additional phase factors originating from the spin degree of freedom that lead to the cancellation of pseudo-orbits with an odd number of reflections at the billiard boundary within a subdomain [72,77]. Especially for the QB an accumulation of peaks is observed around the length of the perimeter, $\mathcal{L}/r_0 = 7.32$, which is reminiscent of whispering gallery modes.

III. GRAPHENE BILLIARDS WITH FOURFOLD SYMMETRY

Due to the symmetry properties of the hexagonal lattice, we cannot proceed as in the case of a GB with C_3 symmetry and construct a GB with fourfold symmetry by cutting a graphene sheet into a shape with that symmetry. Indeed, when rotating an armchair edge of a square GB, the simplest example of such a shape, by $\frac{\pi}{2}$ it will not be mapped into an armchair edge but into a zigzag edge, and vice versa. Nevertheless, at the band edges a GB constructed in this way will have the same spectral properties as the nonrelativistic QB of corresponding shape and thus will exhibit the features outlined in Sec. II. However, when increasing energy, that is, moving away from the band edges, the lattice structure starts to prevail, leading to the occurrence of the Van Hove singularities and the Dirac point, and the absence of the fourfold symmetry becomes noticeable in the properties of the eigenvalues and eigenfunctions. Note that in that energy range the removal of a single site from a GB with a discrete rotational symmetry suffices to lift degeneracies [72]. Therefore we constructed the GB by filling one subdomain with a honeycomb lattice, as illustrated in the left part of Fig. 8, and then rotating it three times by $\frac{\pi}{2}$ about the right-angled corner yielding the GB shown in the right part of Fig. 8. The sites of the two interpenetrating triangular sublattices forming the hexagonal lattice are marked by blue and red dots, respectively, and a unit cell consists of two adjacent sites, i.e., of one site from each sublattice. The subdomains are terminated along the cut lines by a zigzag and armchair edge, respectively. Along the common borders the lattice has a discontinuity, which can be seen in the zoom into that region in the right part of Fig. 8. The distance between the lines formed by the centers of sites along the zigzag edge of a subdomain and along the armchair edge of the adjacent subdomain, respectively, shown as green lines in Fig. 8, is $0.366d_0$, with d_0 denoting the distance between adjacent sites in the honeycomb lattice.

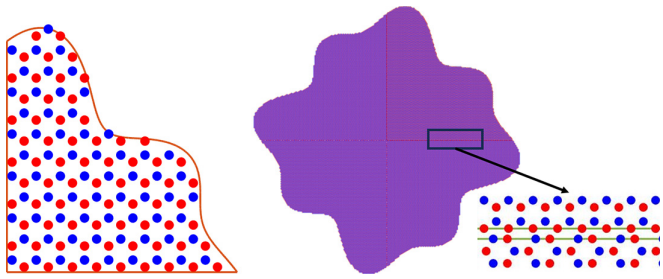

FIG. 8. Left: One fundamental domain of the fourfold-symmetric GB. Right: The full GB is generated by rotating the fundamental domain three times by $\frac{\pi}{2}$ about the right-angled corner. The total number of sites of the GB is 129 196. A zoom into the region of two adjacent fundamental domains illustrates the lattice structure. The green lines connecting the sites along the edges of the two subdomains, which correspond to a zigzag and an armchair edge, respectively, are drawn to guide the eye.

To obtain the eigenvalues and wave functions of the GB, we used the TBM [43], with on-site potential $t_0 = 0$, considering only next-nearest-neighbor hopping, where the size of the corresponding hopping parameter is inversely proportional to the distances d_{ij} between the lattice sites i and j, $t_{1;ij} = td_0/d_{ij}$. It equals t in the bulk of the subdomains. Along the cut lines only hoppings between sites i, j with distance $d_{ij} \leqslant d_0$ are considered. Here, we chose $t = 3$ in the computations. Furthermore, we use Dirichlet BCs along the outer boundary; see Ref. [43].

The elements of the TBM Hamiltonian are given by

$$\hat{\mathcal{H}}_{ij}^{\mathrm{TB}} = t_0\delta_{ij} + t_{1;ij}\tilde{\delta}(|\boldsymbol{r}_i - \boldsymbol{r}_j| - d_{ij})$$

with $\boldsymbol{r}_i$ denoting the location of site i and $\tilde{\delta}(x)$ equal to unity for $x = 0$ and zero otherwise. Assuming that each subdomain

comprises N sites, the TBM Hamiltonian is a $4N \times 4N$ dimensional matrix which can be brought to the form

$$\hat{\mathcal{H}}^{\mathrm{TB}} = \begin{pmatrix} \hat{H} & \hat{V} & 0 & \hat{V}^T \\ \hat{V}^T & \hat{H} & \hat{V} & 0 \\ 0 & \hat{V}^T & \hat{H} & \hat{V} \\ \hat{V} & 0 & \hat{V}^T & \hat{H} \end{pmatrix}. \tag{14}$$

Here, the Hamiltonians $\hat{H}$ of the subdomains are identical, and the matrix $\hat{V}$ and its transpose, $\hat{V}^T$, account for the coupling between the sites along the edges of two adjacent subdomains. By applying a unitary transformation $\hat{U}^\dagger \hat{\mathcal{H}}^{\mathrm{TB}} \hat{U}$ with

$$\hat{U} = \frac{1}{2} \begin{pmatrix} \mathbb{1}_N & \mathbb{1}_N & \mathbb{1}_N & \mathbb{1}_N \\ \mathbb{1}_N & -i\mathbb{1}_N & -\mathbb{1}_N & i\mathbb{1}_N \\ \mathbb{1}_N & -\mathbb{1}_N & \mathbb{1}_N & -\mathbb{1}_N \\ \mathbb{1}_N & i\mathbb{1}_N & -\mathbb{1}_N & -i\mathbb{1}_N \end{pmatrix}, \tag{15}$$

where $\mathbb{1}_N$ denotes the N-dimensional unit matrix, $\hat{\mathcal{H}}^{\mathrm{TB}}$ is brought to block-diagonal form,

$$\hat{U}^\dagger \hat{\mathcal{H}}^{\mathrm{TB}} \hat{U} = \begin{pmatrix} \hat{H}^{\mathrm{TB}(0)} & 0_N & \hat{0}_N & \hat{0}_N \\ \hat{0}_N & \hat{H}^{\mathrm{TB}(1)} & \hat{0}_N & \hat{0}_N \\ \hat{0}_N & \hat{0}_N & \hat{H}^{\mathrm{TB}(2)} & \hat{0}_N \\ \hat{0}_N & \hat{0}_N & \hat{0}_N & \hat{H}^{\mathrm{TB}(3)} \end{pmatrix}.$$

$$\begin{aligned} \hat{H}^{\mathrm{TB}(0)} &= \hat{H} + [\hat{V} + \hat{V}^T], \\ \hat{H}^{\mathrm{TB}(2)} &= \hat{H} - [\hat{V} + \hat{V}^T], \\ \hat{H}^{\mathrm{TB}(1)} &= \hat{H} - i[\hat{V} - \hat{V}^T], \\ \hat{H}^{\mathrm{TB}(3)} &= \hat{H} + i[\hat{V} - \hat{V}^T]. \end{aligned} \tag{16}$$

Each block corresponds to one of the irreducible symmetry classes labeled by $l = 0, 1, 2, 3$ for fourfold rotational symmetry. The transformation properties under rotation by $\frac{\pi}{2}$ of the eigenvectors are given in Eq. (8); that is, those of $\hat{H}^{\mathrm{TB}(0)}$ are rotationally invariant. Furthermore, $\hat{H}^{\mathrm{TB}(0)}$ and $\hat{H}^{\mathrm{TB}(2)}$ are real matrices, whereas $\hat{H}^{\mathrm{TB}(1)}$ and $\hat{H}^{\mathrm{TB}(3)}$ are complex conjugate to each other and thus have the same eigenvalues. Accordingly, the spectrum of $\hat{\mathcal{H}}^{\mathrm{TB}}$ consists of two subspectra of singlets and two identical subspectra of doublets.

We chose $r_0 = 230$ and $d_0 = 1$ so that a honeycomb lattice with $N = 32\,299$ sites fits into each subdomain. The TBM Hamiltonian was diagonalized separately for each symmetry class. The density of states (DOS) $\rho(f) = \frac{1}{N} \sum_{n=1}^{N} \delta(f - f_n)$, with f_n denoting the eigenfrequencies, is shown in Fig. 9 only for the singlets with $l = 0$ (red dots), because it is indistinguishable from those for the other symmetry classes. The black solid curve shows the smoothed DOS, which is obtained by replacing the δ functions by Lorentzians of finite width Γ_L,

$$\rho^{\mathrm{smooth}}(f) = \frac{\pi}{N} \sum_m \frac{\Gamma_{\mathrm{L}}}{(f - f_m)^2 + \Gamma_{\mathrm{L}}^2}, \tag{17}$$

where we chose $\Gamma_{\mathrm{L}} = 0.01$. The peak at the Dirac point at $f/t = 0$ results from the edge states that are localized at the zigzag edges of the outer boundary, and depending on the size of the hopping parameters between the sites of adjacent subdomains, also at zigzag edges along these cut lines.

Examples of wave functions of the GB are shown in Fig. 10 for the four subspaces around the lowest band edge, Van Hove singularities, and Dirac point. They are indistinguishable for the symmetry classes $l = 1, 3$. In the vicinity of the Dirac point, they may have a high intensity at the zigzag edges of the outer boundary and also along the cut lines, whereas around the Van Hove singularities they are localized along interior zigzag edges, leading to the one-dimensional stripe structure. In some cases the wave functions change abruptly around the cut lines. We checked that, nevertheless, they are continuous there.

The corresponding momentum distributions are exhibited in Fig. 11. They are obtained from the Fourier transform of the wave functions from configurational space (x, y) to

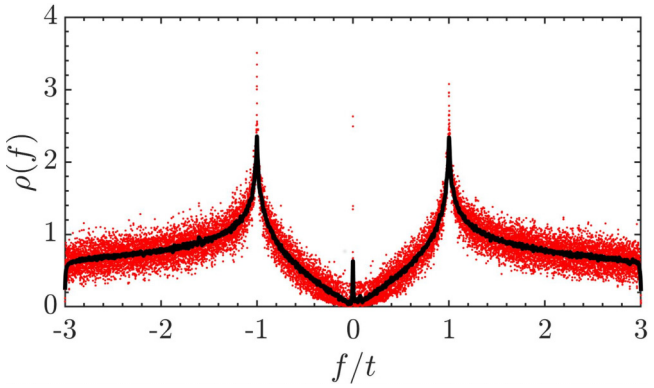

FIG. 9. Density of states of the singlets of the GB. It consists of $4N = 129\,196$ sites. The DOS (red dots) has two Van Hove singularities at $f = \pm t$ and a peak at the Dirac point due to edge states localized at the zigzag edges of the GB. The black curve shows the smoothed DOS.

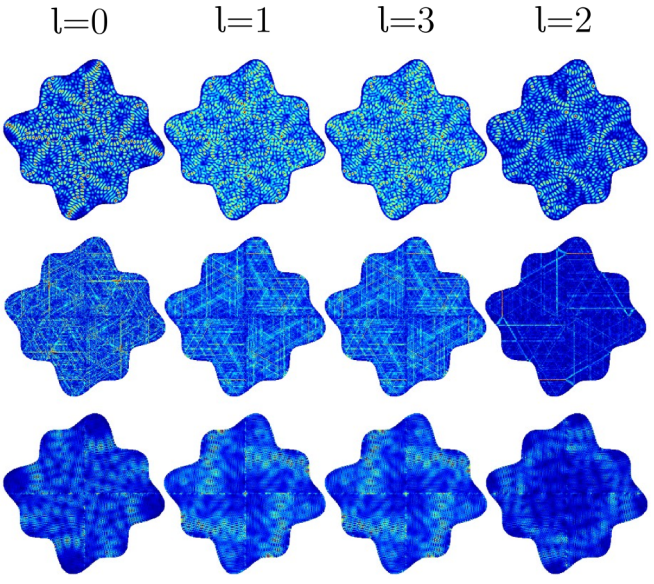

FIG. 10. Intensity distributions of the wave functions of the GB corresponding to eigenstates with eigenvalue k_n around the band edge ($n = 66$, first row), the lower Van Hove singularity ($n = 5168$, second row), and the Dirac point ($n = 6897$, third row) for, from left to right, $l = 0, 1, 3, 2$. The color code changes from dark blue for vanishing intensity to red at the maximum value.

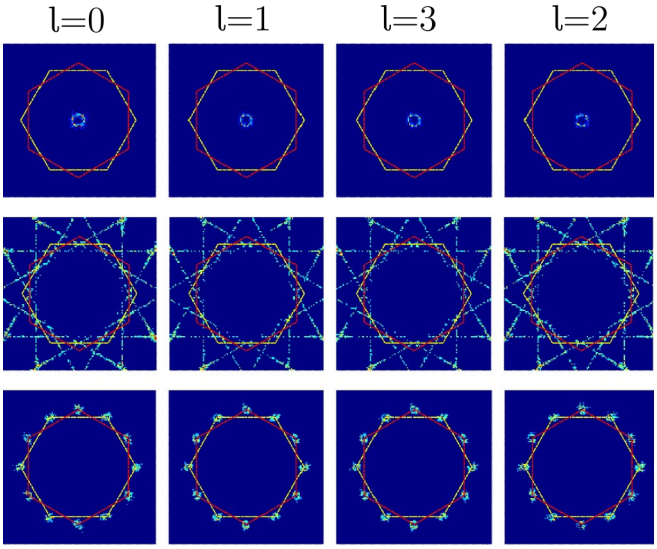

FIG. 11. Similiar to Fig. 10, but for the momentum distributions. The first Brillouin zone is composed of two hexagonal ones that are rotated by $\frac{\pi}{6}$ with respect to each other.

quasimomentum space (q_x, q_y) [43],

$$\Psi(q_x, q_y) = \int_\Omega \Psi(x, y) e^{-i(q_x x + q_y y)} dx dy. \tag{18}$$

To guide the eye, we also show the first Brillouin zone of a honeycomb lattice (red lines) and a copy of it, which is rotated by 30° with respect to it (orange lines). Indeed, the momentum distribution clearly demonstrates that the band structure of propagating modes $f(q_x, q_y)$ exhibits 12 saddle points and 12 Dirac points. Namely, near the band edges the momentum distributions are peaked along circles around the Γ point at the center of the hexagons, where the band terminates, whereas close to the Van Hove singularities they are localized along the isoenergy lines connecting respectively six of the saddle points located at the centers between the corners of the hexagons. In the vicinity of the Dirac points, they are nonzero only at the corners of the hexagons, i.e., at the 12 Dirac points.

We analyzed the spectral properties of the singlets and doublets around the band edges (first row of Fig. 11) and the Dirac point (third row of Fig. 11) obtained from 1600 and 780 eigenvalues for each symmetry class, respectively. Since the DOS is symmetric with respect to the Dirac point, we considered only the eigenvalues at the lower band edge and above the Dirac point. Here, we excluded the edge states, that is, the frequency range of the peak of the DOS around $f = 0$. These are nonuniversal due to the localization properties of the associated wave functions and thus lead to deviations from RMT predictions [43,44]. For the unfolding, we proceeded as in Ref. [72]; namely, we ordered the eigenvalues by size, $E_i \leqslant E_{i+1}$, and shifted them such that $E_1 = 0$, $\tilde{E}_i = E_i - E_1$. Then we replaced them by the smooth part of the integrated spectral density, $\epsilon_i = N^{\rm smooth}(k_i)$ with k_i denoting the effective wave numbers, where $k_i = \sqrt{\tilde{E}_i}$ at the band edge and $k_i = \tilde{E}_i$ at the Dirac point. The smooth part $N^{\rm smooth}(k_i)$ was determined by fitting a second-order polynomial to $N(k_i)$ around

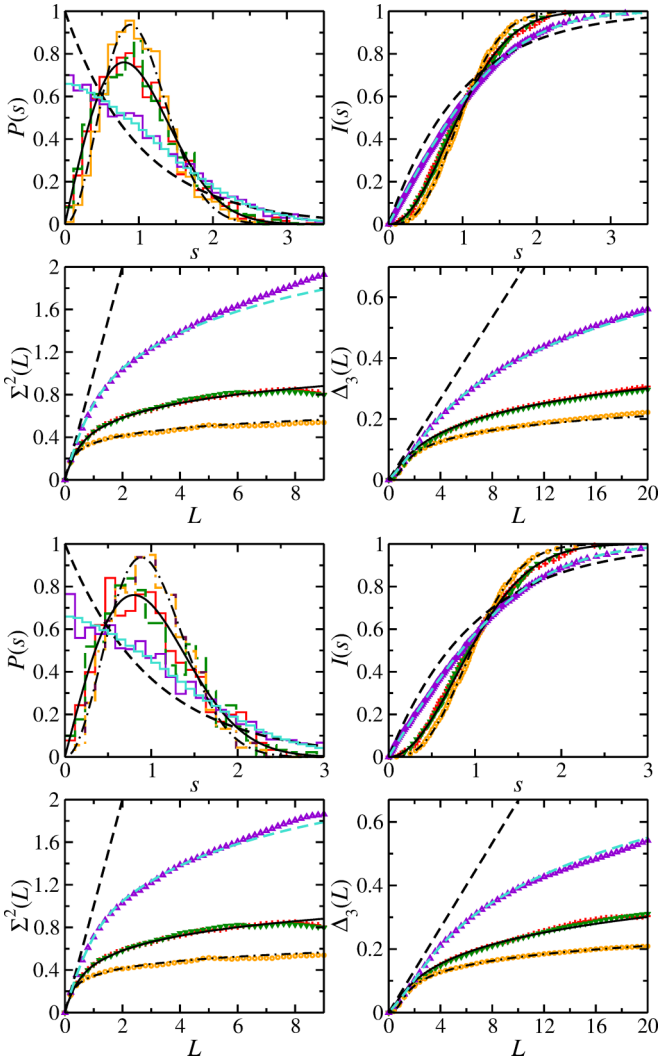

FIG. 12. Upper four panels: Same as Figs. 3(a)–3(d), but for the GB around the lower band edge. Lower four panels: Same as Figs. 3(a)–3(d), but for the GB around the Dirac point.

the band edge [43] and a straight line to it around the Dirac point.

Figure 12 shows the spectral properties for the singlets and doublets around the band edges (upper four panels in Fig. 12) and Dirac point (lower four panels in Fig. 12), and Fig. 13 exhibits the corresponding distributions of the ratios [85,86] of the nonunfolded eigenvalues. Agreement with GOE statistics for the singlets and with GUE statistics for the doublets is very good. Furthermore, we show in Figs. 12–14 results for the spectral properties obtained when taking into account all eigenvalues. They are well described by those of the superimposed spectra of two GOEs and one GUE. Note that this good agreement and also that for the symmetry-projected eigenstates with RMT predictions were achieved after extraction of contributions from nonuniversal orbits, such as the shortest connected periodic orbits shown in Fig. 1, that manifest themselves as slow oscillations $N^{\rm osc}(k_i)$ in the fluctuating part of $N(k_i)$, $N^{\rm fluc}(k_i) = N(k_i) - N^{\rm smooth}(k_i)$. Their contributions are removed by proceeding as in Refs. [72,79,93] and replacing k_i by $\epsilon_i = N^{\rm smooth}(k_i) + N^{\rm osc}(k_i)$. The corresponding length

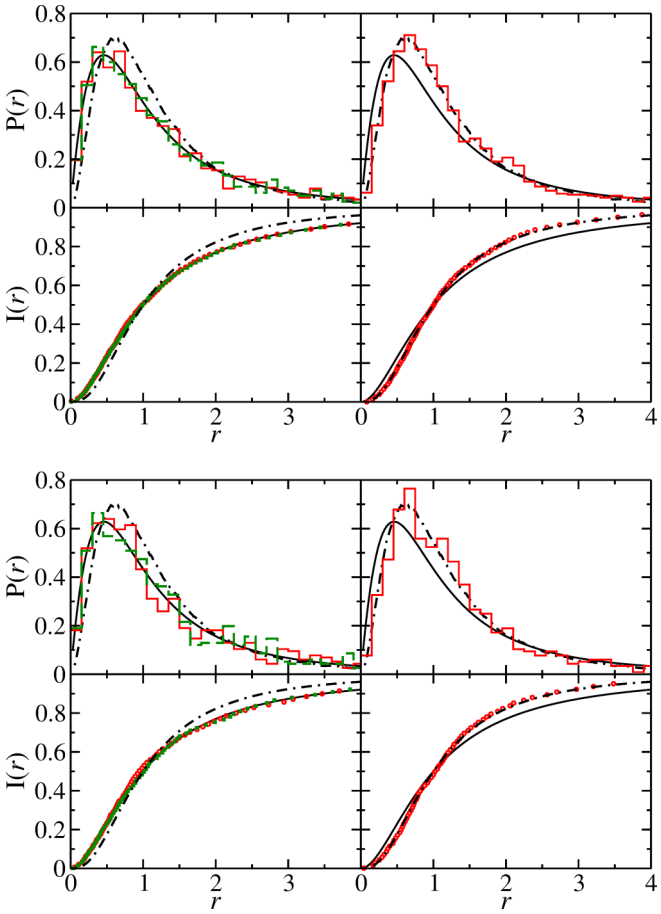

FIG. 13. Upper four panels: Same as Figs. 3(e)–3(h), but for the GB around the lower band edge. Lower four panels: Same as Figs. 3(e)–3(h), but for the GB around the Dirac point.

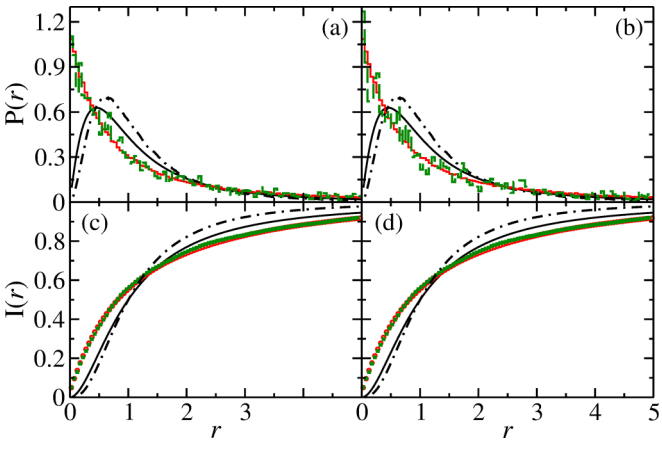

FIG. 14. Ratio distributions $P(r)$ and cumulative ratio distributions $I(r)$ for the GB for all eigenstates (a) and (c) around the band edge and (b) and (d) around the Dirac point (green histogram and squares). They are compared with the results for block-diagonal matrices comprising two matrices from the GOE and one from the GUE (red histogram and circles), and with GUE (black dash-dotted curves) and GOE (black solid curves) statistics.

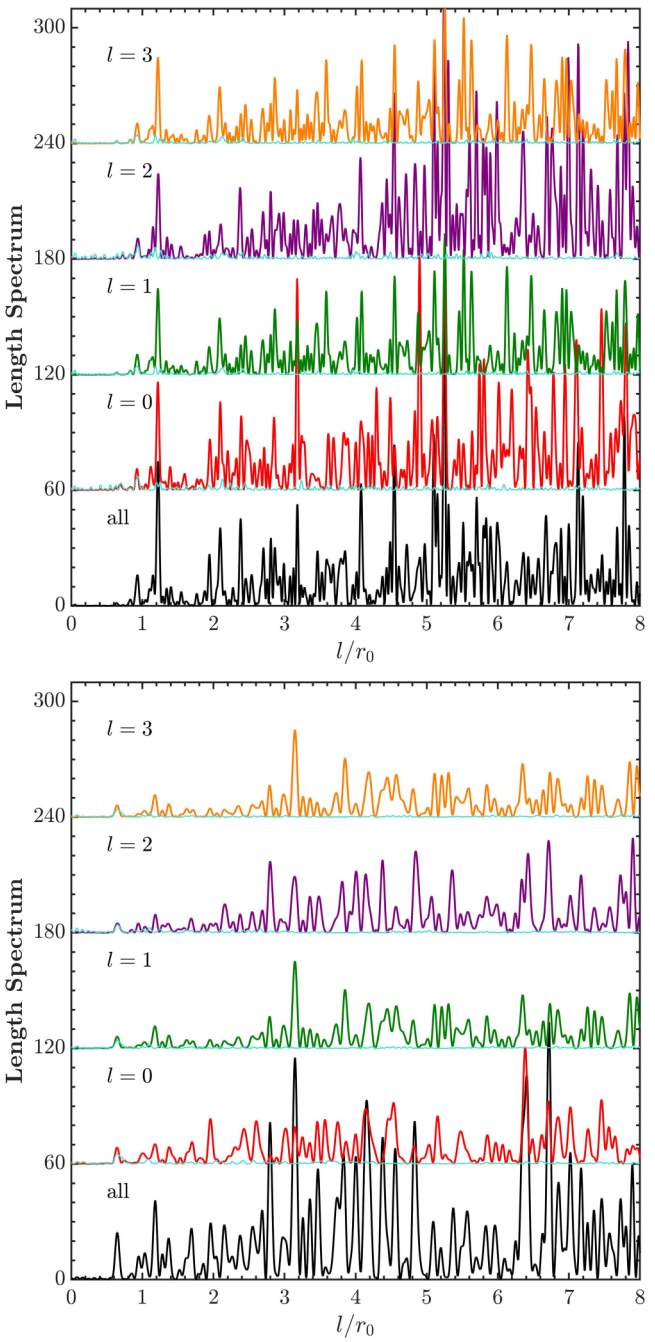

FIG. 15. Top: Comparison of the length spectra of, from bottom to top, the GB (black curve) around the band edge for $l = 0$ (red curve), $l = 1$ (green curve), $l = 2$ (violet curve), and $l = 3$ (orange curve). The cyan curve is obtained from the Fourier transform of the slow oscillations in the fluctuating part of the DOS. Bottom: Same as the top panel, but around the Dirac point.

spectra, deduced from the Fourier transform of $\rho^{\rm osc}(k) = d/dkN^{\rm osc}(k)$, are shown as cyan-colored curves in Fig. 15 together with those computed from the eigenvalues of each of the subspectra around the lower band edge (top panel in Fig. 15) and around the Dirac point (bottom panel in Fig. 15). In distinction to the length spectra of the NB and QB, those of the GB and the symmetry-projected states exhibit peaks of considerable height below $l/r_0 \approx 2$. They are also present in

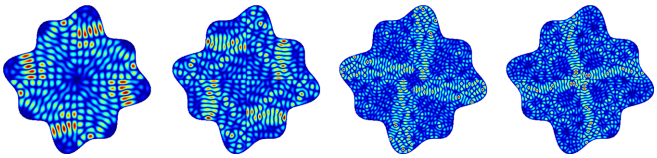

FIG. 16. Intensity distributions of the wave functions of the GB with eigenstate numbers $n = 84, 140, 346, 350$ corresponding to rotationally invariant eigenstates with $l = 0$, which are scarred around a disconnected orbit bouncing back and forth between the cut lines and the billiard boundary, and cross orbits.

the length spectra obtained by taking into account all eigenvalues, implying that they do not correspond to pseudo-orbits, but to orbits bouncing back and forth between the cut lines and the boundary, and thus are due to the lattice structure of the GB. This is illustrated in Fig. 16, where we show in the first two examples wave functions that are localized around these orbits. The patterns are more pronounced than in the corresponding QB, thus corroborating the idea that deviations from GOE and GUE behavior and from the results for the QB originate from such additional orbits. From the good agreement of the spectral properties with those of a QB with fourfold symmetry we may conclude that the GB, which is constructed by coupling four identical finite-size honeycomb lattices, corresponds to one system and not four independent ones.

IV. A POSSIBLE EXPERIMENTAL REALIZATION

A possible experimental realization of GBs with fourfold symmetry consists of superconducting microwave photonic crystals. These were successfully used to emulate the spectral properties of GBs with the shapes of a rectangle, an Africa billiard [43,44,94], and a billiard with threefold symmetry [45,72] and, generally, have been employed for more than a decade to investigate universal features of finite-size and extended artificial graphene structures [26,41,42,95,96]. The construction of the DB with fourfold symmetry is similar to that in Ref. [45], where experiments were performed with a DB whose shape has a C_3 symmetry. A sketch of the DB is shown in Fig. 17. The design used in the COMSOL MULTIPHYSICS simulations consists of a flat cavity made of a perfect-electric-conductor material, which has a height 3 mm and contains metallic cylinders arranged on a triangular grid. Below the cutoff frequency for the first transverse-electric mode, $f^{\text{cutoff}} = 50$ GHz, the electric-field strength is perpendicular to the top and bottom of the resonator and fulfills Dirichlet BCs along the sidewall and at the walls of the cylinders, implying that there the Helmholtz equation is mathematically identical to the Schrödinger equation of a QB [73–75] with circular holes at the positions of the cylinders. The honeycomb structure is formed by the voids encircled by, respectively, three cylinders [41], marked by red and cyan dots in Fig. 17. The resonator wall, shown in orange in Fig. 17, passes through voids implying Dirichlet BCs at the corresponding sites of the honeycomb structure. The eigenfrequencies and associated electric-field strengths were obtained with COMSOL MULTIPHYSICS. We chose r_0 defined in Eq. (4) as $r_0 = 30a_L/\sqrt{3}$, the distance between the lines connecting the sites along the edges of adjacent subdomains as $0.366a_L/\sqrt{3}$,

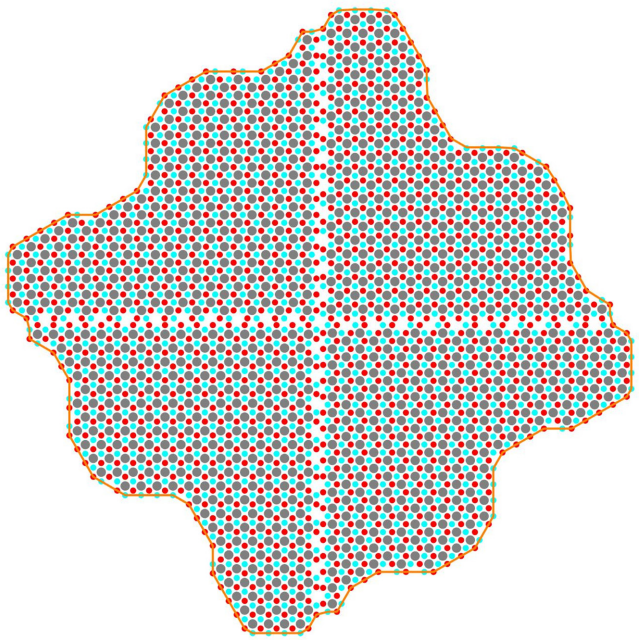

FIG. 17. Sketch of the design of the DB with fourfold symmetry used in the simulations with COMSOL MULTIPHYSICS. It contains 960 metallic cylinders (gray disks) arranged on a triangular grid. The number of sites located on a honeycomb lattice, marked by red and cyan dots, equals 2208. They are positioned at the voids formed by three metallic cylinders. The honeycomb lattice is terminated by zigzag and armchair edges and corresponds to the sites in the GB.

and the radius of the cylinders as $a_L/6$ with $a_L = 12$ mm denoting the lattice constant, yielding $N = 9046$ eigenmodes with eigenfrequencies f_m below 50 GHz.

Generally, for sufficiently large f^{cutoff}, that is, for sufficiently low height, the band structure of propagating modes of such DBs exhibits two Dirac points, where the first and second, respectively, the fourth and fifth bands touch each other conically, and a nearly flat third band. It was shown in Ref. [97] that it is well described by a TBM for a lat-

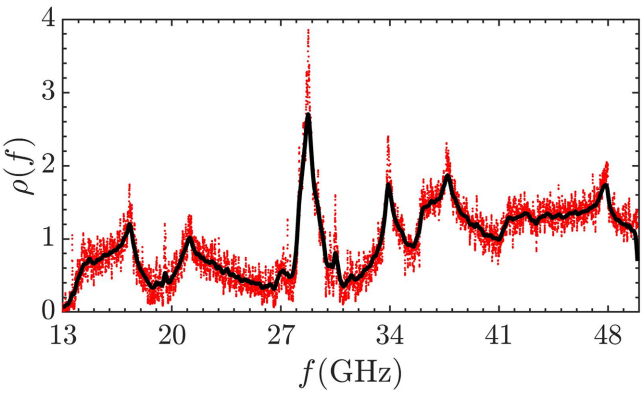

FIG. 18. Density of states of the DB. It exhibits Dirac points at ≈19 GHz and ≈35 GHz that are framed by peaks corresponding to Van Hove singularities and a broadened flat band of high spectral density at $f \simeq 29$ GHz. Above the frequency of the upper Dirac point the DOS is distorted by adjacent bands of partly high spectral density [72].

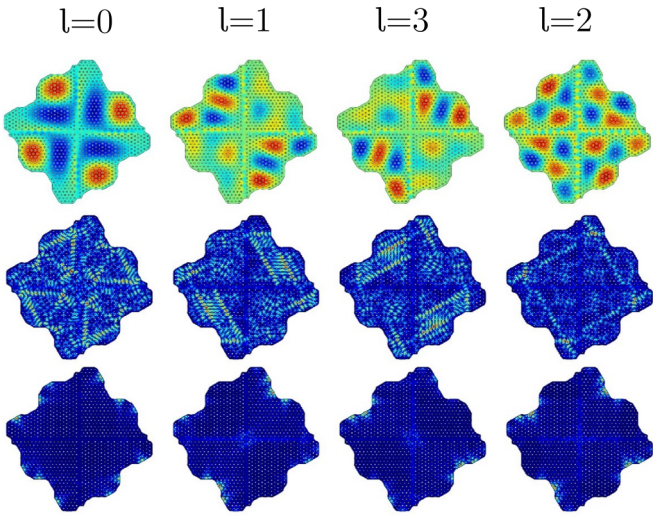

FIG. 19. Electric-field distribution in the DB corresponding to eigenstates with the number n corresponding to the eigenfrequency f_n (see main text). Shown are, from left to right, the following: in the first row, distributions for $n = 9, 18, 19, 22$ at the lower band edge; in the second row, intensity distributions for $n = 676, 678, 679, 677$ around the lower Van Hove singularity, and in the third row, intensity distributions for $n = 999, 1000, 1001, 1002$ around the lower Dirac point. The columns from left to right correspond to $l = 0$, linear combinations of $l = 1$ and $l = 3$, which yield real electric-field distributions, and $l = 2$. In the first row the color code changes from dark blue for the minimum value to red at the maximal value of the electric field. Otherwise the color code is the same as in Fig. 10.

tice consisting of a combination of a honeycomb and a kagome sublattice [45,72,98–101], where the sites of the kagome lattice are at the centers between adjacent cylinders [97]. This was confirmed numerically and experimentally in Refs. [45,102] for a DB with threefold symmetry. The DOS of the DB, which is shown in Fig. 18 together with

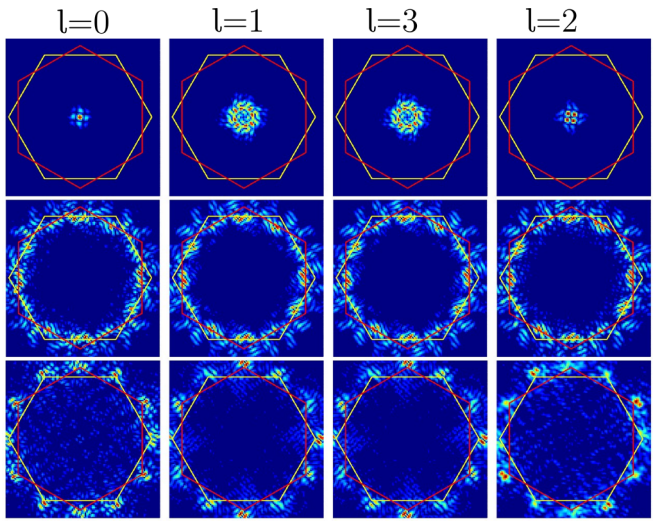

FIG. 20. Similar to Fig. 19, but for the momentum distributions. Here, we used the complex-valued eigenmodes corresponding to $l = 1$ and $l = 3$. The first Brillouin zone is composed of two hexagonal ones that are rotated by $\frac{\pi}{6}$ with respect to each other.

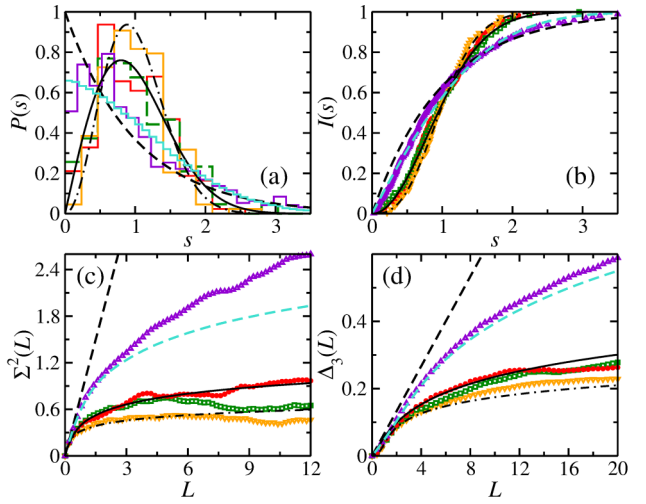

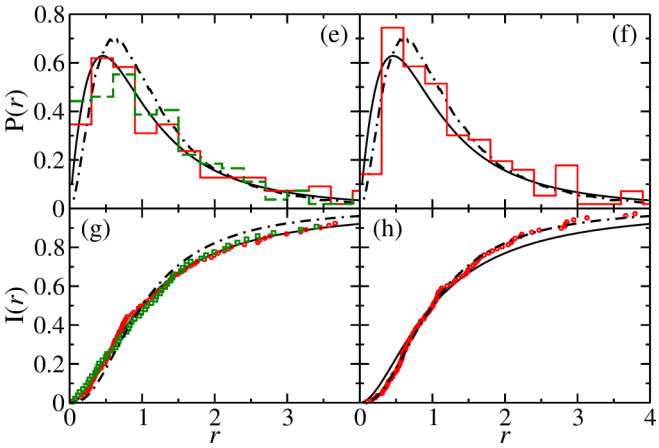

FIG. 21. (a)–(h) Same as Fig. 3, but for the subspectra of the DB, with each of them comprising 185 eigenfrequencies.

the smoothed DOS (black curve), obtained from Eq. (17) with $\Gamma_L = 0.1$, indeed has the same structure as that of a honeycomb-kagome lattice. It exhibits Dirac points at $f \approx 19$ GHz and $f \approx 35$ GHz that are framed by Van Hove singularities, and a broadened flat band of high spectral density around $f \approx 29$ GHz. The increased DOS in the vicinity of the Dirac points originates from edge states localized at zigzag edges along the cut lines and the outer boundary. Below the flat band the properties of DBs are well captured by a TBM for the GB of corresponding shape [43–45,95]. We consider only that region in the following.

In Fig. 19 we show examples for intensity distributions of the electric-field strength. The wave functions of the first and fourth columns belong to the two singlet groups with $l = 0$ and $l = 2$, respectively. The second and third columns show real-valued superpositions of the electric-field distributions for $l = 1$ and $l = 3$. As in Fig. 10, in some cases the distributions seem to be discontinuous along the cut lines. We checked that this is not the case. The structure of the electric-field patterns is similar to that exhibited by the wave functions of the GB. In Fig. 20 are plotted the corresponding momentum distributions. Here, we used the complex-valued electric-field modes corresponding to $l = 1$ (second column of Fig. 20) and

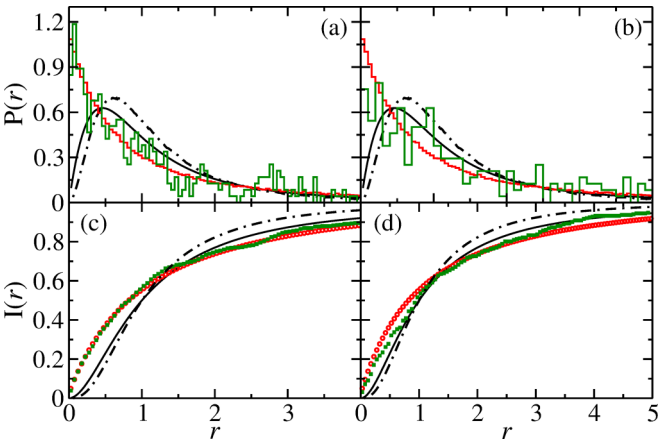

FIG. 22. Ratio distributions $P(r)$ and cumulative ratio distributions $I(r)$ for the DB for all eigenstates (a) and (c) around the band edge, comprising 560 eigenfrequencies, and (b) and (d) around the Dirac point, containing 265 eigenfrequencies (green histogram and squares). They are compared with the results for block-diagonal matrices comprising two matrices from the GOE and one from the GUE (red histogram and circles) and GUE (black dash-dotted curves) statistics.

$l = 3$ (third column of Fig. 20). As for the GB (see Fig. 11), they are peaked close to the lower band edge around the center of the first Brillouin zone, near the lower Van Hove singularity around the isoenergy lines connecting the saddle points and near the frequencies of the Dirac points at the corners of the hexagons.

Around the band edge we were able to separate the spectrum which was obtained with COMSOL MULTIPHYSICS into the subspectra of, respectively, 185 singlets and nearly degenerate doublets based on electric-field intensity distributions and by checking the fluctuating part of the integrated spectral density, which exhibits jumps when there are missing or spurious eigenfrequencies [45]. Around the Dirac point, in total 265 eigenfrequencies could be identified. For the unfolding we proceeded as in Sec. III. In Fig. 21 we show results for the spectral properties around the lower band edge for the eigenfrequencies corresponding to $l = 0, 1, 2$, and in Fig. 22 we show the ratio distributions for all eigenstates irrespective of their symmetry classes around the lower band edge [Figs. 22(a) and 22(c)] and the Dirac point [Figs. 22(b) and 22(d)]. Deviations from the expected RMT results are attributed to contributions of electric-field modes, which are localized along short periodic orbits. Examples are shown in Fig. 23. Hence the spectral properties and the electric-field distributions of the DB exhibit similar features to the eigenvalues and wave functions of the GB.

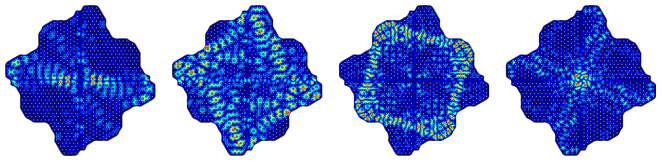

FIG. 23. Intensity distributions of the electric field in the DB corresponding to $n = 148, 193$ and $l = 1$ and $n = 497, 518$ and $l = 0$.

V. CONCLUSION

We realize a GB whose boundary has a fourfold rotational symmetry. This is done by constructing a honeycomb-lattice sheet which has the shape of one-quarter of the GB and rotating it four times about the right-angled corner. The GB has defect lines along the common boundaries of two adjacent subdomains, which are terminated there by a zigzag edge and an armchair edge, respectively. The dynamics of the corresponding CB is chaotic. The eigenstates are computed separately for each symmetry class. For this the TBM Hamiltonian is brought to the form given in Eq. (16). We demonstrate that the spectral properties comply in the regions around the band edges and Dirac point with those of the QB of corresponding shape, i.e., with the RMT predictions for quantum systems with fourfold symmetry and a chaotic classical counterpart. Here, we excluded eigenstates, whose eigenfunctions are localized at zigzag edges along the boundary and the cut lines, that lead to the peak of exceptionally high DOS around the Dirac points in Figs. 9 and 18 and are nonuniversal. More precisely, in the region around the Dirac point, no agreement is found with those of the relativistic NB of corresponding shape, even though there the excitation energies of graphene are effectively described by the same Dirac equation (2). This is attributed to the backscattering at the billiard boundary, which leads to a mixing of valley states. This is corroborated by the momentum distributions of the symmetry-projected eigenstates which are peaked at all corners of the first Brillouin zone in that energy range. Actually, the momentum distributions reveal that the first Brillouin zone is formed by two hexagonal ones that are rotated by 30° with respect to each other. We propose an experimental setup consisting of a DB and perform COMSOL MULTIPHYSICS computations. These confirm that the DB provides an appropriate system to investigate experimentally the properties of the eigenvalues and wave functions of the GB of corresponding shape. Generally, a GB whose shape has a discrete rotational symmetry can be constructed by cutting a graphene sheet to its shape, if it complies with that of the hexagonal lattice. We demonstrate, using a GB with fourfold rotational symmetry, that, if this is not the case, the GB can be constructed by gluing together sheets with the shape of a subdomain and that the properties of their eigenstates agree with those of quantum systems with the same symmetry properties, despite the unavoidable defect lines. The same procedure can be used for GBs whose shape has an M-fold symmetry with $M > 4$; however, with increasing number of defect lines, deviations from RMT predictions will become noticeable.

ACKNOWLEDGMENTS

This work was supported by the NSF of China under Grants No. 11775100, No. 12247101, and No. 11961131009. W.Z. acknowledges financial support from the China Scholarship Council (Grant No. CSC-202106180044). We acknowl-

edge financial support from the Institute for Basic Science in Korea through Project No. IBS-R024-D1.

APPENDIX A: THE BOUNDARY-INTEGRAL EQUATIONS FOR QBs AND NBs

The eigenvalues of the QB and NB were obtained from the corresponding boundary-integral equations (BIEs). For the QB the BIE is given by [88]

$$u(\varphi') = \int_0^{2\pi} d\varphi |w'(\varphi)| Q^{\mathrm{QB}}(k;\varphi,\varphi') u(\varphi) \tag{A1}$$

$$= \hat{Q}^{\mathrm{QB}}(k) u(\varphi'), \tag{A2}$$

with

$$Q^{\mathrm{QB}}(k;\varphi,\varphi') = i\frac{k}{2}\cos[\alpha(\varphi') - \xi(\varphi,\varphi')] H_1^{(1)}(k\rho), \tag{A3}$$

where $H_m^{(1)}(k\rho) = J_m(k\rho) + iY_m(k\rho)$ is the Hankel function of the first kind of order m, $u(s) = \partial_n \psi(s)$ denotes the normal derivative of the wave function $\psi(s)$, s refers to the arclength parameter,

$$s(\varphi) = \int_0^{\varphi} |w'(\tilde{\varphi})| d\tilde{\varphi}, \quad s \in [0, \mathcal{L}), \quad ds = |w'(\varphi)| d\varphi \tag{A4}$$

with $w'(\varphi) = \frac{dw(\varphi)}{d\varphi}$ and $\mathcal{L}$ being the perimeter, and

$$e^{i\xi(\varphi,\varphi')} = \frac{w(\varphi) - w(\varphi')}{|w(\varphi) - w(\varphi')|}, \quad \rho(\varphi,\varphi') = |w(\varphi) - w(\varphi')|. \tag{A5}$$

The BIEs for the two wave-function components of a NB can be written in the form

$$\boldsymbol{\psi}^{\dagger}[\boldsymbol{r}(\varphi')] = \oint_{\partial\Omega} d\varphi |w'(\varphi)| e^{i\frac{\Delta\Phi(\varphi,\varphi')}{2}} \hat{Q}^{\mathrm{NB}}[k;\boldsymbol{r}(\varphi'),\boldsymbol{r}(\varphi)] \boldsymbol{\psi}^{\dagger}[\boldsymbol{r}(\varphi)]$$

$$= \hat{\boldsymbol{Q}}^{\mathrm{NB}}(k) \boldsymbol{\psi}^{\dagger}[\boldsymbol{r}(\varphi)], \tag{A6}$$

where we introduced the notations $\Delta\Phi(\varphi,\varphi') = \frac{\alpha(\varphi') - \alpha(\varphi)}{2}$ and $\hat{\boldsymbol{Q}}_{ij}^{\mathrm{NB}}(k) = \hat{\boldsymbol{Q}}_j^{\mathrm{NB}}(k)\delta_{ij}$. The integral operator $\hat{\boldsymbol{Q}}_j^{\mathrm{NB}}(k)$ is applied to $\psi_j^*(\varphi)$ to obtain $\psi_j^*(\varphi')$. For the first component the BIE is given by

$$\psi_1^*(\varphi') = \int_0^{2\pi} d\varphi |w'(\varphi)| e^{i\frac{\Delta\Phi(\varphi,\varphi')}{2}} Q_1^{\mathrm{NB}}(k;\varphi,\varphi') \psi_1^*(\varphi), \tag{A7}$$

$$Q_1^{\mathrm{NB}}(k;\varphi,\varphi') = i\frac{k}{2}\left\{ i\sin\left(\frac{\Delta\Phi(\varphi,\varphi')}{2}\right) H_0^{(1)}(k\rho) + \cos\left(\frac{\alpha(\varphi') + \alpha(\varphi)}{2} - \xi(\varphi,\varphi')\right) H_1^{(1)}(k\rho)\right\}. \tag{A8}$$

The corresponding equations for $\psi_2^*(\varphi')$ and $Q_2^{\mathrm{NB}}(k;\varphi,\varphi')$ are obtained with Eq. (3) by multiplying the integrand with $e^{-i\Delta\Phi(\varphi,\varphi')}$.

To compute the symmetry-projected eigenstates, the BIE is separated into individual BIEs for each symmetry class. This is done for a billiard with M-fold symmetry by employing the periodicity properties

$$w\left(\varphi + \lambda\frac{2\pi}{M}\right) = e^{i\lambda\frac{2\pi}{M}} w(\varphi), \tag{A9}$$

$$w'\left(\varphi + \lambda\frac{2\pi}{M}\right) = e^{i\lambda\frac{2\pi}{M}} w'(\varphi), \tag{A10}$$

$$e^{i\alpha\left(\varphi + \lambda\frac{2\pi}{M}\right)} = e^{i\lambda\frac{2\pi}{M}} e^{i\alpha(\varphi)}, \tag{A11}$$

with $\lambda = 0, 1, 2, \ldots, M-1$ to restrict the integration range of φ and φ' to one fundamental domain, $\varphi, \varphi' \in [0, \frac{2\pi}{M})$, yielding the BIEs

$$u^{(l)}(\varphi') = \int_0^{\frac{2\pi}{M}} d\varphi \tilde{Q}^{(l)}(k;\varphi,\varphi') u^{(l)}(\varphi) \tag{A12}$$

with $l = 0, 1, , 2, \ldots, M-1$ and $u^{(l)}(\varphi) = \partial_n \psi^{(l)}(\varphi)$ for the QB and $u^{(l)}(\varphi) = \psi^{(l)*}(\varphi)$ for the NB.

$$\tilde{Q}^{(l)}(k;\varphi,\varphi') = \sum_{\lambda=0}^{M-1} e^{i\frac{2l\pi}{M}\lambda} \tilde{M}_{\lambda}(k;\varphi,\varphi'), \tag{A13}$$

where

$$\tilde{M}_{\lambda}(k;\varphi,\varphi') = \tilde{Q}\left(k;\varphi + \lambda\frac{2\pi}{M},\varphi'\right). \tag{A14}$$

Here, $\tilde{Q}$ stands for Q^{QB}, Q_1^{NB}, or Q_2^{NB}.

APPENDIX B: TRACE FORMULA FOR FOURFOLD-SYMMETRIC QBs AND NBs

The derivation of the trace formula of a typical fourfold-symmetric QB with a chaotic classical dynamics and of the corresponding NB starts from the BIEs [77,103,104] given in Eqs. (A1)–(A3), (A6)–(A8), and (A12). These equations have nontrivial solutions at the zeros of the spectral determinant

$$\det(\mathbb{1} - \hat{\boldsymbol{Q}}^{(l)}(k)) = 0. \tag{B1}$$

Here, $\hat{\boldsymbol{Q}}$ stands for $\hat{Q}^{\mathrm{QB}}$ defined in Eq. (A1) or $\hat{\boldsymbol{Q}}^{\mathrm{NB}}$ given in Eq. (A6). The spectral density is obtained from [103,105]

$$\rho(k) = \rho^{\mathrm{smooth}}(k) - \frac{1}{\pi}\mathrm{Im}\frac{d}{dk}\ln\det[\mathbb{1} - \hat{\boldsymbol{Q}}^{(l)}(k)]$$

$$= \rho^{\mathrm{smooth}}(k) + \frac{1}{\pi}\mathrm{Im}\sum_{p=1}^{\infty}\frac{1}{p}\frac{d}{dk}[\mathrm{Tr}(\hat{\boldsymbol{Q}}^{(l)})^p(k)], \tag{B2}$$

with

$$\mathrm{Tr}(\hat{\boldsymbol{Q}}^{(l)})^p(k) = \oint_{\partial\bar{\Omega}} ds_1 \oint_{\partial\bar{\Omega}} ds_2 \cdots \oint_{\partial\bar{\Omega}} ds_p \mathcal{P}_p, \tag{B3}$$

where we introduced the abbreviations $s_r = s(\varphi_r)$ with $s_{p+1} = s_1$, and $\partial\bar{\Omega}$ denotes the boundary of one subdomain, i.e., of the symmetry-reduced configurational space of the billiard. For the QB, $\mathcal{P}_p$ is obtained from Eq. (A3),

$$\mathcal{P}_p = \prod_{r=1}^{p} Q^{\mathrm{QB}(l)}[k;\boldsymbol{r}(\varphi_r),\boldsymbol{r}(\varphi_{r+1})], \tag{B4}$$

and for the massless NB from Eq. (A8),

$$\mathcal{P}_p = 2\cos\left(\sum_{r=1}^{p}\frac{\Delta\Phi(\varphi_{r+1},\varphi_r)}{2}\right) \times \prod_{r=1}^{p} Q_1^{\mathrm{NB}(l)}[k;\boldsymbol{r}(\varphi_r),\boldsymbol{r}(\varphi_{r+1})]. \tag{B5}$$

To obtain the symmetry-projected trace formulas, we replace $\hat{\boldsymbol{Q}}^{(l)} = Q^{\mathrm{QB}(l)}, Q_1^{\mathrm{NB}(l)}$ by the sums in Eq. (A13),

$$\prod_{r=1}^{p} Q^{(l)}[k;\boldsymbol{r}(\varphi_r),\boldsymbol{r}(\varphi_{r+1})] = \prod_{r=1}^{p}\left\{\sum_{\lambda=0}^{3} e^{il\frac{\pi}{2}\lambda} M_\lambda(k;\varphi_r,\varphi_{r+1})\right\} = \sum_{\lambda=0}^{3} e^{il\frac{\pi}{2}\lambda}\mathcal{M}_\lambda^{p(l)}(k;\{\varphi_i\}), \tag{B6}$$

with

$$\mathcal{M}_\lambda^{p(l)}(k;\{\varphi_i\}) = \sum_{N_0=1}^{p}\sum_{N_1=1}^{p}\sum_{N_2=1}^{p}\sum_{N_3=1}^{p}\tilde{\delta}(N_0+N_1+N_2+N_3-p)\tilde{\delta}\left(\left\{[N_1+2N_2+3N_3]\frac{\pi}{2}\right\}\mathrm{modulo}(2\pi)-\lambda\right)$$
$$\times\sum_{\{\pi_r\}}\prod_{r=1}^{N_0} M_0(k;\varphi_{\pi_r},\varphi_{\pi_{r+1}})\prod_{r=N_0+1}^{N_0+N_1} M_1(k;\varphi_{\pi_r},\varphi_{\pi_{r+1}})\prod_{r=N_0+N_1+1}^{N_0+N_1+N_2} M_2(k;\varphi_{\pi_r},\varphi_{\pi_{r+1}})\prod_{r=N_0+N_1+N_2+1}^{p} M_3(k;\varphi_{\pi_r},\varphi_{\pi_{r+1}}). \tag{B7}$$

Here, the sum over $\{\pi_r\} = \{\pi_1,\pi_2,\ldots,\pi_p\}$ is over all permutations π of $\{1,2,\ldots,p\}$.

The integrals in Eq. (B3) can be solved in the semiclassical limit $\hbar\to 0$ or $k\to\infty$ with $\hbar k$ fixed. For this we replace the Hankel functions in Eqs. (A3) and (A8) and the corresponding one for $\psi_2^*(\varphi')$ by their asymptotic values for $k\to\infty$ [106] and extract them from $\mathcal{M}_\lambda^{p(l)}(k;\{\varphi_i\})$,

$$H_0(k\rho_{r+1,r}) \simeq \sqrt{\frac{2}{\pi\rho_{r+1,r}}}e^{ik\rho_{r+1,r}-\frac{i}{4}\pi}, \tag{B8}$$

$$H_1(k\rho_{r+1,r}) \simeq \frac{1}{i}H_0(k\rho_{r+1,r}), \tag{B9}$$

with $\rho_{r+1,r} = \rho(\varphi_{r+1},\varphi_r)$. Inserting these asymptotic approximations of the Hankel functions into Eq. (B7), in the semiclassical limit each of the summands of $\mathcal{M}_\lambda^{p(l)}(k;\{\varphi_i\})$ in Eq. (B7) can be split into a factor $\bar{\mathcal{M}}_\lambda^{p(l)}(\{\varphi_i\})$, which does not depend on k and $\hbar$, and an integral over the product of the semiclassical approximations for $H_0(k\rho_{r+1,r})$ [77,104],

$$\mathrm{Tr}(\hat{\boldsymbol{Q}}^{(l)})^p(k) \simeq \sum_{\lambda=0}^{2} e^{il\frac{\pi}{2}\lambda}\sum_{N_0=1}^{p}\sum_{N_1=1}^{p}\sum_{N_2=1}^{p}\sum_{N_3=1}^{p}\tilde{\delta}(N_0+N_1+N_2+N_3-p)$$
$$\times\tilde{\delta}\left(\left\{[N_1+2N_2+3N_3]\frac{\pi}{2}\right\}\mathrm{modulo}(2\pi)-\lambda\right)\sum_{\{\pi_r\}}\left(\frac{i}{4}k\right)^p\bar{\mathcal{M}}_\lambda^{N_0,N_1,N_2,N_3}(\{\varphi_{\pi_r}\})$$
$$\times\sum_{\{\pi_r\}}\oint_{\partial\bar{\Omega}}ds_1\cdots\oint_{\partial\bar{\Omega}}ds_p\prod_{r=1}^{p}\left[\sqrt{\frac{2}{\pi\rho_{r+1,r}}}e^{ik\rho_{r+1,r}-\frac{i}{4}\pi}\right]. \tag{B10}$$

The p integrals are performed by applying the stationary phase approximation [103]. In the semiclassical limit the nonvanishing contributions to $\mathrm{Tr}(\hat{\boldsymbol{Q}}^{(l)})^p(k)$ are periodic orbits of order p complying with the symmetry class l. They are the same as in the usual Gutzwiller trace formula for periodic orbits in the fundamental domain, and we can use the results of Refs. [81,82,103] to obtain, for the symmetry-projected trace, the formula

$$\rho^{(l)\mathrm{fluc}}(k) = \frac{1}{\pi}\mathrm{Re}\sum_{\gamma_p^l}\sum_{\lambda=0}^{3} e^{il\frac{\pi}{2}\lambda}\mathcal{A}_{\gamma_p^l}e^{i\Theta_{\gamma_p^l}} \tag{B11}$$

for the QB [81,82] and

$$\rho^{(l)\mathrm{fluc}}(k) = \frac{1}{\pi}\mathrm{Re}\sum_{\gamma_p^l}(-1)^p\cos\left(\Phi_{\gamma_p^l}\right)\cos\left(p\frac{\pi}{2}\right)$$
$$\times\sum_{\lambda=0}^{3} e^{il\frac{\pi}{2}\lambda}\mathcal{A}_{\gamma_p^l}e^{i\Theta_{\gamma_p^l}} \tag{B12}$$

for the NB.

The sum over γ_p^l stands for the sums over N_0, N_1, N_2, and N_3 yielding periodic orbits with p reflections at the boundary and is over all orbits which are p periodic in the fundamental domain corresponding to the irreducible representation l. Furthermore, $\mathcal{A}_{\gamma_p^l}$ and $\Theta_{\gamma_p^l}$ denote amplitudes and phases as in the usual Gutzwiller trace formula with

$$\mathcal{A}_{\gamma_p^l} = \frac{l_{\mathrm{PO}}^{(l,p)}}{r_{\mathrm{PO}}^{(l,p)}\sqrt{\left|\mathrm{Tr}M_{\mathrm{PO}}^{(l,p)}-2\right|}},$$

$$\Theta_{\gamma_p^l} = kl_{\mathrm{PO}}^{(l,p)} - \frac{\pi}{2}\mu_{\mathrm{PO}}^{(l,p)}, \tag{B13}$$

with $l_{\mathrm{PO}}^{(l,p)}$, $\mu_{\mathrm{PO}}^{(l,p)}$, and $M_{\mathrm{PO}}^{(l,p)}$ being the length, Maslov index, and monodromy matrix of the periodic orbit and $r_{\mathrm{PO}}^{(l,p)}$ being the number of repetitions of the primitive periodic orbit in the respective fundamental domain. Note that these orbits are not necessarily periodic after unfolding them to the full system. For the NB, periodic orbits with an odd p cancel out. Thus, as in the full massless NB, only periodic orbits with an even

number of reflections [21,107] contribute to the trace formula. This feature originates from the chirality property and the additional spin degree of freedom, i.e., the vectorial character of the Dirac equation [21,90,108].

[1] Y. G. Sinai, Dynamical systems with elastic reflections, Russ. Math. Surv. **25**, 137 (1970).

[2] L. A. Bunimovich, On the ergodic properties of nowhere dispersing billiards, Commun. Math. Phys. **65**, 295 (1979).

[3] M. V. Berry, Regularity and chaos in classical mechanics, illustrated by three deformations of a circular 'billiard', Eur. J. Phys. **2**, 91 (1981).

[4] M. V. Berry and R. J. Mondragon, Neutrino billiards: Time-reversal symmetry-breaking without magnetic fields, Proc. R. Soc. London A **412**, 53 (1987).

[5] D. P. DiVincenzo and E. J. Mele, Self-consistent effective-mass theory for intralayer screening in graphite intercalation compounds, Phys. Rev. B **29**, 1685 (1984).

[6] K. S. Novoselov, A. K. Geim, S. V. Morozov, D. Jiang, Y. Zhang, S. V. Dubonos, I. V. Grigorieva, and A. A. Firsov, Electric field effect in atomically thin carbon films, Science **306**, 666 (2004).

[7] A. Geim and K. Novoselov, The rise of graphene, Nat. Mater. **6**, 183 (2007).

[8] P. Avouris, Z. Chen, and V. Perebeinos, Carbon-based electronics, Nat. Nanotechnol. **2**, 605 (2007).

[9] F. Miao, S. Wijeratne, Y. Zhang, U. C. Coskun, W. Bao, and C. N. Lau, Phase-coherent transport in graphene quantum billiards, Science **317**, 1530 (2007).

[10] L. A. Ponomarenko, F. Schedin, M. I. Katsnelson, R. Yang, E. W. Hill, K. S. Novoselov, and A. K. Geim, Chaotic Dirac billiard in graphene quantum dots, Science **320**, 356 (2008).

[11] C. W. J. Beenakker, Colloquium: Andreev reflection and Klein tunneling in graphene, Rev. Mod. Phys. **80**, 1337 (2008).

[12] X. Zhang and Z. Liu, Extremal transmission and beating effect of acoustic waves in two-dimensional sonic crystals, Phys. Rev. Lett. **101**, 264303 (2008).

[13] A. H. Castro Neto, F. Guinea, N. M. R. Peres, K. S. Novoselov, and A. K. Geim, The electronic properties of graphene, Rev. Mod. Phys. **81**, 109 (2009).

[14] D. Abergel, V. Apalkov, J. Berashevich, K. Ziegler, and T. Chakraborty, Properties of graphene: A theoretical perspective, Adv. Phys. **59**, 261 (2010).

[15] S. R. Zandbergen and M. J. A. de Dood, Experimental observation of strong edge effects on the pseudodiffusive transport of light in photonic graphene, Phys. Rev. Lett. **104**, 043903 (2010).

[16] M. Dresselhaus, G. Dresselhaus, and P. Eklund, *Science of Fullerenes and Carbon Nanotubes* (Academic, San Diego, CA, 1996).

[17] S. Reich, J. Maultzsch, C. Thomsen, and P. Ordejón, Tight-binding description of graphene, Phys. Rev. B **66**, 035412 (2002).

[18] P. R. Wallace, The band theory of graphite, Phys. Rev. **71**, 622 (1947).

[19] A. R. Akhmerov and C. W. J. Beenakker, Detection of valley polarization in graphene by a superconducting contact, Phys. Rev. Lett. **98**, 157003 (2007).

[20] A. R. Akhmerov and C. W. J. Beenakker, Boundary conditions for Dirac fermions on a terminated honeycomb lattice, Phys. Rev. B **77**, 085423 (2008).

[21] J. Wurm, K. Richter, and İ. Adagideli, Edge effects in graphene nanostructures: From multiple reflection expansion to density of states, Phys. Rev. B **84**, 075468 (2011).

[22] J. C. Slonczewski and P. R. Weiss, Band structure of graphite, Phys. Rev. **109**, 272 (1958).

[23] M. Polini, F. Guinea, M. Lewenstein, H. C. Manoharan, and V. Pellegrini, Artificial graphene as a tunable Dirac material, Nat. Nanotechnol. **8**, 625 (2013).

[24] P. V. Parimi, W. T. Lu, P. Vodo, J. Sokoloff, J. S. Derov, and S. Sridhar, Negative refraction and left-handed electromagnetism in microwave photonic crystals, Phys. Rev. Lett. **92**, 127401 (2004).

[25] S. Joannopoulos, J. D. Johnson, R. Meade, and J. Winn, *Photonic Crystals: Molding the Flow of Light* (Princeton University Press, Princeton, 2008).

[26] S. Bittner, B. Dietz, M. Miski-Oglu, P. Oria Iriarte, A. Richter, and F. Schäfer, Observation of a Dirac point in microwave experiments with a photonic crystal modeling graphene, Phys. Rev. B **82**, 014301 (2010).

[27] U. Kuhl, S. Barkhofen, T. Tudorovskiy, H.-J. Stöckmann, T. Hossain, L. de Forges de Parny, and F. Mortessagne, Dirac point and edge states in a microwave realization of tight-binding graphene-like structures, Phys. Rev. B **82**, 094308 (2010).

[28] A. Singha, M. Gibertini, B. Karmakar, S. Yuan, M. Polini, G. Vignale, M. I. Katsnelson, A. Pinczuk, L. N. Pfeiffer, K. W. West, and V. Pellegrini, Two-dimensional Mott-Hubbard electrons in an artificial honeycomb lattice, Science **332**, 1176 (2011).

[29] L. Nádvorník, M. Orlita, N. A. Goncharuk, L. Smrčka, V. Novák, V. Jurka, K. Hruška, Z. Výborný, Z. R. Wasilewski, M. Potemski, and K. Výborný, From laterally modulated two-dimensional electron gas towards artificial graphene, New J. Phys. **14**, 053002 (2012).

[30] K. K. Gomes, W. Mar, W. Ko, F. Guinea, and H. C. Manoharan, Designer Dirac fermions and topological phases in molecular graphene, Nature (London) **483**, 306 (2012).

[31] L. Tarruell, D. Greif, T. Uehlinger, G. Jotzu, and T. Esslinger, Creating, moving and merging Dirac points with a Fermi gas in a tunable honeycomb lattice, Nature (London) **483**, 302 (2012).

[32] T. Uehlinger, G. Jotzu, M. Messer, D. Greif, W. Hofstetter, U. Bissbort, and T. Esslinger, Artificial graphene with tunable interactions, Phys. Rev. Lett. **111**, 185307 (2013).

[33] M. C. Rechtsman, Y. Plotnik, J. M. Zeuner, D. Song, Z. Chen, A. Szameit, and M. Segev, Topological creation and destruction of edge states in photonic graphene, Phys. Rev. Lett. **111**, 103901 (2013).

[34] M. C. Rechtsman, J. M. Zeuner, A. Tünnermann, S. Nolte, M. Segev, and A. Szameit, Strain-induced pseudomagnetic

field and photonic Landau levels in dielectric structures, Nat. Photonics **7**, 153 (2013).
[35] A. B. Khanikaev, S. H. Mousavi, W.-K. Tse, M. Kargarian, A. H. MacDonald, and G. Shvets, Photonic topological insulators, Nat. Mater. **12**, 233 (2013).
[36] X. Wang, H. T. Jiang, C. Yan, F. S. Deng, Y. Sun, Y. H. Li, Y. L. Shi, and H. Chen, Transmission properties near Dirac-like point in two-dimensional dielectric photonic crystals, Europhys. Lett. **108**, 14002 (2014).
[37] Z. Shi, G. Lin, T.-H. Xiao, H.-L. Guo, and Z.-Y. Li, All-optical modulation of a graphene-cladded silicon photonic crystal cavity, Photonics **2**, 1513 (2015).
[38] M. Bellec, U. Kuhl, G. Montambaux, and F. Mortessagne, Topological transition of Dirac points in a microwave experiment, Phys. Rev. Lett. **110**, 033902 (2013).
[39] M. Bellec, U. Kuhl, G. Montambaux, and F. Mortessagne, Tight-binding couplings in microwave artificial graphene, Phys. Rev. B **88**, 115437 (2013).
[40] M. Bellec, U. Kuhl, G. Montambaux, and F. Mortessagne, Manipulation of edge states in microwave artificial graphene, New J. Phys. **16**, 113023 (2014).
[41] S. Bittner, B. Dietz, M. Miski-Oglu, and A. Richter, Extremal transmission through a microwave photonic crystal and the observation of edge states in a rectangular Dirac billiard, Phys. Rev. B **85**, 064301 (2012).
[42] B. Dietz, F. Iachello, M. Miski-Oglu, N. Pietralla, A. Richter, L. von Smekal, and J. Wambach, Lifshitz and excited-state quantum phase transitions in microwave Dirac billiards, Phys. Rev. B **88**, 104101 (2013).
[43] B. Dietz, T. Klaus, M. Miski-Oglu, and A. Richter, Spectral properties of superconducting microwave photonic crystals modeling Dirac billiards, Phys. Rev. B **91**, 035411 (2015).
[44] B. Dietz, T. Klaus, M. Miski-Oglu, A. Richter, M. Wunderle, and C. Bouazza, Spectral properties of Dirac billiards at the van Hove singularities, Phys. Rev. Lett. **116**, 023901 (2016).
[45] W. Zhang, X. Zhang, J. Che, M. Miski-Oglu, and B. Dietz, Properties of eigenmodes and quantum-chaotic scattering in a superconducting microwave Dirac billiard with threefold rotational symmetry, Phys. Rev. B **107**, 144308 (2023).
[46] M. V. Berry and M. Tabor, Calculating the bound spectrum by path summation in action-angle variables, J. Phys. A: Math. Gen. **10**, 371 (1977).
[47] M. Robnik and G. Veble, On spectral statistics of classically integrable systems, J. Phys. A: Math. Gen. **31**, 4669 (1998).
[48] O. Bohigas, M. J. Giannoni, and C. Schmit, Characterization of chaotic quantum spectra and universality of level fluctuation laws, Phys. Rev. Lett. **52**, 1 (1984).
[49] M. L. Mehta, *Random Matrices* (Academic, San Diego, CA, 1990).
[50] *Chaos and Quantum Physics*, edited by M. Giannoni, A. Voros, and J. Zinn-Justin (Elsevier, Amsterdam, 1989).
[51] T. Guhr, A. Müller-Groeling, and H. A. Weidenmüller, Random-matrix theories in quantum physics: Common concepts, Phys. Rep. **299**, 189 (1998).
[52] F. Haake, S. Gnutzmann, and M. Kuś, *Quantum Signatures of Chaos* (Springer-Verlag, Heidelberg, 2018).
[53] M. V. Berry and M. Tabor, Level clustering in the regular spectrum, Proc. R. Soc. London A **356**, 375 (1977).
[54] G. Casati, F. Valz-Gris, and I. Guarnieri, On the connection between quantization of nonintegrable systems and statistical theory of spectra, Lett. Nuovo Cimento **28**, 279 (1980).
[55] J. Güttinger, C. Stampfer, S. Hellmüller, F. Molitor, T. Ihn, and K. Ensslin, Charge detection in graphene quantum dots, Appl. Phys. Lett. **93**, 212102 (2008).
[56] J. Güttinger, T. Frey, C. Stampfer, T. Ihn, and K. Ensslin, Spin states in graphene quantum dots, Phys. Rev. Lett. **105**, 116801 (2010).
[57] J. Wurm, A. Rycerz, İ. Adagideli, M. Wimmer, K. Richter, and H. U. Baranger, Symmetry classes in graphene quantum dots: Universal spectral statistics, weak localization, and conductance fluctuations, Phys. Rev. Lett. **102**, 056806 (2009).
[58] L. Huang, Y.-C. Lai, and C. Grebogi, Relativistic quantum level-spacing statistics in chaotic graphene billiards, Phys. Rev. E **81**, 055203(R) (2010).
[59] A. Rycerz, Random matrices and quantum chaos in weakly disordered graphene nanoflakes, Phys. Rev. B **85**, 245424 (2012).
[60] A. Rycerz, Strain-induced transitions to quantum chaos and effective time-reversal symmetry breaking in triangular graphene nanoflakes, Phys. Rev. B **87**, 195431 (2013).
[61] P. Yu, Z.-Y. Li, H.-Y. Xu, L. Huang, B. Dietz, C. Grebogi, and Y.-C. Lai, Gaussian orthogonal ensemble statistics in graphene billiards with the shape of classically integrable billiards, Phys. Rev. E **94**, 062214 (2016).
[62] P. Yu, W. Zhang, B. Dietz, and L. Huang, Quantum signatures of chaos in relativistic quantum billiards with shapes of circle- and ellipse-sectors, J. Phys. A: Math. Theor. **55**, 224015 (2022).
[63] F. Leyvraz, C. Schmit, and T. H. Seligman, Anomalous spectral statistics in a symmetrical billiard, J. Phys. A: Math. Gen. **29**, L575 (1996).
[64] C. Dembowski, H.-D. Gräf, A. Heine, H. Rehfeld, A. Richter, and C. Schmit, Gaussian unitary ensemble statistics in a time-reversal invariant microwave triangular billiard, Phys. Rev. E **62**, R4516(R) (2000).
[65] C. Dembowski, B. Dietz, H.-D. Gräf, A. Heine, F. Leyvraz, M. Miski-Oglu, A. Richter, and T. H. Seligman, Phase shift experiments identifying Kramers doublets in a chaotic superconducting microwave billiard of threefold symmetry, Phys. Rev. Lett. **90**, 014102 (2003).
[66] O. Knill, On nonconvex caustics of convex billiards, Elem. Math. **53**, 89 (1998).
[67] B. Gutkin, Dynamical "breaking" of time reversal symmetry, J. Phys. A: Math. Theor. **40**, F761 (2007).
[68] G. Veble, T. Prosen, and M. Robnik, Expanded boundary integral method and chaotic time-reversal doublets in quantum billiards, New J. Phys. **9**, 15 (2007).
[69] B. Dietz, T. Guhr, B. Gutkin, M. Miski-Oglu, and A. Richter, Spectral properties and dynamical tunneling in constant-width billiards, Phys. Rev. E **90**, 022903 (2014).
[70] L. G. C. Rego, A. Gusso, and M. G. E. da Luz, Anomalous quantum chaotic behaviour in suspended electromechanical nanostructures, J. Phys. A: Math. Gen. **38**, L639 (2005).
[71] A. Gusso, M. G. E. da Luz, and L. G. C. Rego, Quantum chaos in nanoelectromechanical systems, Phys. Rev. B **73**, 035436 (2006).

[72] W. Zhang and B. Dietz, Microwave photonic crystals, graphene, and honeycomb-kagome billiards with threefold symmetry: Comparison with nonrelativistic and relativistic quantum billiards, Phys. Rev. B **104**, 064310 (2021).
[73] H.-J. Stöckmann and J. Stein, "Quantum" chaos in billiards studied by microwave absorption, Phys. Rev. Lett. **64**, 2215 (1990).
[74] S. Sridhar, Experimental observation of scarred eigenfunctions of chaotic microwave cavities, Phys. Rev. Lett. **67**, 785 (1991).
[75] H.-D. Gräf, H. L. Harney, H. Lengeler, C. H. Lewenkopf, C. Rangacharyulu, A. Richter, P. Schardt, and H. A. Weidenmüller, Distribution of eigenmodes in a superconducting stadium billiard with chaotic dynamics, Phys. Rev. Lett. **69**, 1296 (1992).
[76] H. Weyl, Elektron und Gravitation. I, Z. Phys. **56**, 330 (1929).
[77] B. Dietz and Z.-Y. Li, Semiclassical quantization of neutrino billiards, Phys. Rev. E **102**, 042214 (2020).
[78] S. C. Creagh and R. G. Littlejohn, Semiclassical trace formulas in the presence of continuous symmetries, Phys. Rev. A **44**, 836 (1991).
[79] M. Sieber, U. Smilansky, S. C. Creagh, and R. G. Littlejohn, Non-generic spectral statistics in the quantized stadium billiard, J. Phys. A: Math. Gen. **26**, 6217 (1993).
[80] J. P. Keating and J. M. Robbins, Discrete symmetries and spectral statistics, J. Phys. A: Math. Gen. **30**, L177 (1997).
[81] J. M. Robbins, Discrete symmetries in periodic-orbit theory, Phys. Rev. A **40**, 2128 (1989).
[82] C. H. Joyner, S. Müller, and M. Sieber, Semiclassical approach to discrete symmetries in quantum chaos, J. Phys. A: Math. Theor. **45**, 205102 (2012).
[83] B. Dietz, Relativistic quantum billiards with threefold rotational symmetry: Exact, symmetry-projected solutions for the equilateral neutrino billiard, Act. Phys. Pol. A **140**, 473 (2021).
[84] H. Weyl, Über die Abhängigkeit der Eigenschwingungen einer Membran und deren Begrenzung, J. Reine Angew. Math. **1912**, 1 (1912).
[85] V. Oganesyan and D. A. Huse, Localization of interacting fermions at high temperature, Phys. Rev. B **75**, 155111 (2007).
[86] Y. Y. Atas, E. Bogomolny, O. Giraud, and G. Roux, Distribution of the ratio of consecutive level spacings in random matrix ensembles, Phys. Rev. Lett. **110**, 084101 (2013).
[87] Y. Atas, E. Bogomolny, O. Giraud, P. Vivo, and E. Vivo, Joint probability densities of level spacing ratios in random matrices, J. Phys. A: Math. Theor. **46**, 355204 (2013).
[88] A. Bäcker, Numerical aspects of eigenvalue and eigenfunction computations for chaotic quantum systems, in *The Mathematical Aspects of Quantum Maps*, edited by M. D. Esposti and S. Graffi (Springer, Berlin, 2003), pp. 91–144.
[89] B. Dietz, Unidirectionality and Husimi functions in constant-width neutrino billiards, J. Phys. A: Math. Theor. **55**, 474003 (2022).
[90] C. Dembowski, B. Dietz, H.-D. Gräf, A. Heine, T. Papenbrock, A. Richter, and C. Richter, Experimental test of a trace formula for a chaotic three-dimensional microwave cavity, Phys. Rev. Lett. **89**, 064101 (2002).
[91] M. C. Gutzwiller, Periodic orbits and classical quantization conditions, J. Math. Phys. **12**, 343 (1971).
[92] M. C. Gutzwiller, *Chaos in Classical and Quantum Mechanics* (Springer, New York, 1990).
[93] B. Dietz, Semi-Poisson statistics in relativistic quantum billiards with shapes of rectangles, Entropy **25**, 762 (2023).
[94] B. Dietz and A. Richter, Quantum and wave dynamical chaos in superconducting microwave billiards, Chaos **25**, 097601 (2015).
[95] B. Dietz, T. Klaus, M. Miski-Oglu, A. Richter, M. Bischoff, L. von Smekal, and J. Wambach, Fullerene C_{60} simulated with a superconducting microwave resonator and test of the Atiyah-Singer index theorem, Phys. Rev. Lett. **115**, 026801 (2015).
[96] F. Iachello, B. Dietz, M. Miski-Oglu, and A. Richter, Algebraic theory of crystal vibrations: Singularities and zeros in vibrations of one- and two-dimensional lattices, Phys. Rev. B **91**, 214307 (2015).
[97] W. Maimaiti, B. Dietz, and A. Andreanov, Microwave photonic crystals as an experimental realization of a combined honeycomb-kagome lattice, Phys. Rev. B **102**, 214301 (2020).
[98] T. Jacqmin, I. Carusotto, I. Sagnes, M. Abbarchi, D. D. Solnyshkov, G. Malpuech, E. Galopin, A. Lemaître, J. Bloch, and A. Amo, Direct observation of Dirac cones and a flatband in a honeycomb lattice for polaritons, Phys. Rev. Lett. **112**, 116402 (2014).
[99] Z. Lan, N. Goldman, and P. Öhberg, Coexistence of spin-$\frac{1}{2}$ and spin-1 Dirac-Weyl fermions in the edge-centered honeycomb lattice, Phys. Rev. B **85**, 155451 (2012).
[100] J.-L. Lu, W. Luo, X.-Y. Li, S.-Q. Yang, J.-X. Cao, X.-G. Gong, and H.-J. Xiang, Two-dimensional node-line semimetals in a honeycomb-kagome lattice, Chin. Phys. Lett. **34**, 057302 (2017).
[101] H. Zhong, Y. Zhang, Y. Zhu, D. Zhang, C. Li, Y. Zhang, F. Li, M. R. Belić, and M. Xiao, Transport properties in the photonic super-honeycomb lattice—a hybrid fermionic and bosonic system, Ann. Phys. (Berlin) **529**, 1600258 (2017).
[102] W. Zhang, X. Zhang, J. Che, J. Lu, M. Miski-Oglu, and B. Dietz, Experimental study of closed and open microwave waveguide graphs with preserved and partially violated time-reversal invariance, Phys. Rev. E **106**, 044209 (2022).
[103] M. Sieber, Semiclassical transition from an elliptical to an oval billiard, J. Phys. A: Math. Gen. **30**, 4563 (1997).
[104] B. Dietz, Circular and elliptical neutrino billiards: A semiclassical approach, Acta Phys. Pol. A **136**, 770 (2019).
[105] M. Sieber, Billiard systems in three dimensions: The boundary integral equation and the trace formula, Nonlinearity **11**, 1607 (1998).
[106] *Handbook of Mathematical Functions with Formulas, Graphs and Mathematical Tables*, edited by M. Abramowitz and I. A. Stegun (Dover, New York, 2013).
[107] J. Bolte and S. Keppeler, A semiclassical approach to the Dirac equation, Ann. Phys. (Amsterdam) **274**, 125 (1999).
[108] R. Balian and B. Duplantier, Electromagnetic waves near perfect conductors. I. Multiple scattering expansions. distribution of modes, Ann. Phys. (Amsterdam) **104**, 300 (1977).